The Astrophysical Journal, 981:91 (20pp), 2025 March 1 https://doi.org/10.3847/1538-4357/adaf18

Swift-XRT and NuSTAR Monitoring of Obscuration Variability in Mrk 477

N. Torres-Albà[1,2,9], Z. Hu[3], I. Cox[1], S. Marchesi[1,4,5], M. Ajello[1], A. Pizzetti[1,6], I. Pal[1], R. Silver[7], and X. Zhao[8]
[1] Department of Physics and Astronomy, Clemson University, Kinard Lab of Physics, Clemson, SC 29634, USA
[2] Department of Astronomy, University of Virginia, P.O. Box 400325, Charlottesville, VA 22904, USA
[3] Department of Physics, University of Miami, Coral Gables, FL 33124, USA
[4] Dipartimento di Fisica e Astronomia (DIFA), Universitá di Bologna, via Gobetti 93/2, I-40129 Bologna, Italy
[5] INAF – Osservatorio di Astrofisica e Scienza dello Spazio di Bologna, Via Piero Gobetti, 93/3, 40129, Bologna, Italy
[6] European Southern Observatory, Alonso de Córdova 3107, Casilla 19, Santiago 19001, Chile
[7] NASA Goddard Space Flight Center, Greenbelt, MD 20771, USA
[8] Department of Astronomy, University of Illinois at Urbana-Champaign, Urbana, IL 61801, USA
Received 2024 November 11; revised 2025 January 23; accepted 2025 January 26; published 2025 February 28

Abstract

We present the analysis of 15 X-ray observations of Mrk 477, a nearby Seyfert 2 active galactic nucleus, with the objective to monitor its obscuring column density variability. The full data set consists of five archival observations, split into two XMM-Newton, two NuSTAR and one Chandra observation, plus two dedicated monitoring campaigns. The monitoring campaigns were performed with Swift-XRT and NuSTAR, containing five observations each. We performed a simultaneous analysis using self-consistent torus models, deriving geometric properties of the torus as well as the obscuration along the line of sight. Mrk 477 is best modeled with a torus with a large covering factor yet low column density (on average). Its line-of-sight column density oscillates between 1.5 and 7×10^{23} cm^{-2}. Mrk 477 presents frequent obscuring column density variability, on timescales as short as ∼2 weeks. The probability of drawing a pair of obscuration-variable observations for Mrk 477 when having two, three, and four observations is 40%, 78%, and 95%, respectively. Adding the results of this work to those of another 26 sources, we find a trend of increasing obscuration variability with time (from ∼20% at $\Delta t < 10$ days, to ∼60%–70% at timescales larger than 5 yr). We discuss whether this is compatible with the majority of obscuration variability coming from broad-line region clouds.

Unified Astronomy Thesaurus concepts: Active galactic nuclei (16); High energy astrophysics (739); Seyfert galaxies (1447); X-ray active galactic nuclei (2035)

1. Introduction

Active galactic nuclei (AGN) are supermassive black holes (SMBHs) that are actively accreting the material that surrounds them. As per the unification theory, all AGN categories are essentially distinguished by only three factors: orientation angle, intrinsic power, and the presence (or lack) of a jet (C. M. Urry & P. Padovani 1995). A key element in this categorization is the torus, a toroidal distribution of material, initially modeled as homogeneous, that surrounds the accreting SMBH, obscuring certain lines of sight. AGN viewed at an edge-on orientation are named Type II AGN, and are generally obscured in X-rays and devoid of broad emission lines, which originate in the broad-line region (BLR).

Later studies, both from an infrared and an X-ray perspective, paint a slightly more complex picture when it comes to the distribution of material in the torus. Spectral energy distribution (SED) fitting in the infrared favors a clumpy material distribution over a homogeneous one (e.g., M. Nenkova et al. 2002; C. Ramos Almeida et al. 2014). Similarly, changes in X-ray obscuration (measured by the obscuring line-of-sight column density, $N_{\rm H,los}$) in nearby AGN support an inhomogeneous torus scenario (e.g., G. Risaliti et al. 2002). $N_{\rm H,los}$ variability has been observed in timescales as short as <1 day (e.g., M. Elvis et al. 2004; G. Risaliti et al. 2009), and as long as years (e.g., A. G. Markowitz et al. 2014). They also span a broad range of $N_{\rm H,los}$, from $\sim 10^{22}$ cm^{-2} (e.g., S. Laha et al. 2020), to Compton-thin/-thick transitions (i.e., changing-look AGN, e.g., G. Risaliti et al. 2005; S. Bianchi et al. 2009; E. Rivers et al. 2015).

Obscuration variability in X-rays is a powerful tool that allows measuring $N_{\rm H,los}$ as a function of time, thus deriving properties of the obscuring clouds through extensive, continuous monitoring campaigns (e.g., A. G. Markowitz et al. 2014). This requires observing a full "eclipsing event"; that is, the ingress and egress of individual clouds into the line of sight However, very few X-ray instruments have the capability to provide this sort of continuous, daily monitoring over the necessary timescales (i.e., years to decades). In fact, the most extensive of such campaigns monitored 55 individual sources (A. G. Markowitz et al. 2014), spanning a total of 230 yr of equivalent observing time with the Rossi X-ray Timing Explorer (K. Jahoda et al. 2006). It resulted in the detection of only eight and four individual eclipsing events in Seyfert 1 and Seyfert 2 galaxies, respectively. Despite the poor statistics, this study is the most complete to date, and has thus been used to calibrate one of the most recent X-ray emission models based on clumpy tori (J. Buchner et al. 2019).

Due to these observing difficulties, works focusing on comparing archival observations, or monitoring campaigns comprised of a few individual observations, are much more common. The $\Delta N_{\rm H,los}$ between two different observations

[9] GECO Fellow.

separated by a given Δt has been used to place upper limits on cloud distances to the SMBH in a number of works (e.g., G. Risaliti et al. 2002, 2005; A. Pizzetti et al. 2022; S. Marchesi et al. 2022).

Only a handful of works exist that systematically analyze larger (i.e., 10–20 sources) samples of AGN. Interestingly, works focusing on Seyfert 2 galaxies all reach a similar conclusion: less than half of nearby obscured AGN show $N_{\rm H,los}$ variability (7/20 sources in S. Laha et al. 2020, 11/25 in L. Hernández-Garcìa et al. 2015, 5/12 sources in N. Torres-Albà et al. 2023, 5/13 in A. Pizzetti et al. 2025). It is currently unclear if such a low fraction of $N_{\rm H,los}$-variable sources is expected by clumpy torus models.

In order to further explore $N_{\rm H,los}$ variability in the local universe, we have started an effort to analyze all archival data of AGN in the sample of X. Zhao et al. (2021) that have multiple soft X-ray observations. This sample was selected because it is comprised by obscured, yet Compton-thin AGN (i.e., $N_{\rm H,los} = 10^{23}$–10^{24} cm^{-2}), making it possible to tightly constrain $N_{\rm H,los}$, while also deriving torus geometrical properties via the usage of recent X-ray torus models (see, e.g., X. Zhao et al. 2021; N. Torres-Albà et al. 2023, for details). Furthermore, all sources contain at least one Nuclear Spectroscopic Telescope Array (NuSTAR) observation (F. A. Harrison et al. 2013, sensitive in the 3–78 keV range), which is necessary to derive the mentioned torus properties. Finally, all sources are detected by Swift-Burst Alert Telescope (BAT), observing in the 15–150 keV range), implying their 15–150 keV flux is $>5 \times 10^{-12}$ erg s^{-1} cm^{-2}, making it likely that archival soft X-ray observations will have high enough number of counts for modeling $N_{\rm H,los}$ variability.[10]

The first 25 sources within the sample, with the highest chance of being $N_{\rm H,los}$ variable, were presented in N. Torres-Albà et al. (2023) and A. Pizzetti et al. (2025). It resulted in only 37% being confidently classified as $N_{\rm H,los}$ variable. As part of this effort, we have also developed a method to quickly flag potential $N_{\rm H,los}$ variability from hardness ratio comparisons of archival observations (I. S. Cox et al. 2023), and are currently working on applying it to the whole of the Chandra archive (I. Cox et al. 2025, in preparation). We have also presented the analysis of particularly interesting sources (NGC 7974 and NGC 6300) (A. Pizzetti et al. 2022, D. Sengupta et al. 2025, in preparation, respectively).

Within this sample, Mrk 477 was further selected for monitoring campaigns for two main reasons: it was already seen to be $N_{\rm H,los}$ variable in X. Zhao et al. (2021), as well as our preliminary analysis of the existent archival data, and it is the brightest source in the sample. In fact, Mrk 477 is the closest/brightest type II quasar, at a distance of 163 Mpc (see, e.g., T. M. Heckman et al. 1997; C. Ramos Almeida et al. 2023, and references therein), making it the perfect source for an inexpensive monitoring campaign.

In this work, we analyze the existing archival data (five observations; two by XMM-Newton, two by NuSTAR, and one by Chandra), as well as the data from two dedicated monitoring campaigns (five observations by Swift-XRT, and five more by NuSTAR). In Section 2, we describe the observations and the data reduction procedures. In Section 3, we describe the spectral analysis methodology and the X-ray torus reflection models used. In Section 4, we present spectra and best-fit parameters for the joint analysis of the 15 observations. In Sections 5 and 6, we present our discussion and conclusions, respectively.

[10] See N. Torres-Albà et al. (2023) and A. Pizzetti et al. (2025) for further details on the sample selection.

2. Observations and Data Reduction

Mrk 477 has been observed in the X-rays a total of 15 times, five of which are archival observations taken before any dedicated monitoring campaigns. Among those, there are two XMM-Newton observations taken 2 days apart in 2010, followed by two NuSTAR observations taken 9 days apart in 2014. Finally, there is a Chandra observation taken in 2015.

Our first dedicated monitoring campaign took place between May and November 2021 (Proposal Number 1720100, Swift Cycle 17, PI: Torres-Albà), and is comprised of five Swift-XRT observations of a total of ∼10 ks each, separated by consecutive time differences such that $\Delta t \simeq 2$ weeks, 1 month, 2 months, 3 months (see Tables 1 and 2 for exact details). The NuSTAR monitoring campaign took place between 2022 December and 2023 June (Cycle 8, PI: Torres-Albà), with five ∼20 ks observations, following the same pattern of time differences between consecutive observations. A summary of observations can be found in Table 1.

All spectra were binned with at least 25 counts per bin in order to use χ^2 statistics for the fitting, with the exception of the Swift-XRT data, which did not have a large enough number of counts. The Swift-XRT data was thus binned with 5 counts per bin, and fit using W-stat instead. We fit the spectra using XSPEC v12.11.1 (K. A. Arnaud 1996, in HEAsoft version 6.28). We took into account Galactic absorption in the line of sight, according to the values measured by P. M. W. Kalberla et al. (2005), as well as the D. A. Verner et al. (1996) photoelectric cross section. We fixed metal abundances to the solar value, using the E. Anders & N. Grevesse (1989) cosmic abundance measurements. All luminosity distances are computed assuming a cosmology with $H_0 = 70$ km s^{-1} Mpc^{-1} and $\Omega_\Lambda = 0.73$.

2.1. XMM-Newton Data Analysis

We used the XMM-Newton Science Analysis Software (XMM-SAS) v20.0.0 to reduce the XMM-Newton data from both MOS1 and MOS2 as well as the PN camera (F. Jansen et al. 2001), adopting the standard procedure, cleaning for flaring periods. Once the event file was cleaned, we extracted the source spectra from a 30″ circular region centered on the source. The background spectra were obtained using a circle of radius 45″, located near the source (avoiding nearby objects as well as CCD lines).

2.2. NuSTAR Data Analysis

The NuSTAR data was retrieved from both NuSTAR Focal Plane Modules (FPMA/B; F. A. Harrison et al. 2013) and processed using the NuSTAR Data Analysis Software (NUSTARDAS) v2.1.2. The Calibration Database (CALDB) v20211020 was run to calibrate the event data files through the `nupipeline` task. We extracted the source and background spectra using the `nuproducts` script. For both FPMA and FPMB we used a circular region with a 50” radius, centered around the source, to extract its spectrum. For the background, we adopted an annulus (inner radius 100”, outer radius 160”) surrounding the source.

Table 1
Summary of All Observations Analyzed in This Work

Date	Observatory	ObsID	Exp. Time (ks)	Counts	Δt (days)
(1)	(2)	(3)	(4)	(5)	(6)
2010-07-21	XMM-Newton	0651100301	7.1	2193	⋯
2010-07-23	XMM-Newton	0651100401	6.5	2157	2
2014-05-15	NuSTAR	60061255002	18.1	4045	1392
2014-05-24	NuSTAR	60061255004	17.1	4604	9
2015-07-06	Chandra	17121	10.1	623	408
2021-05-01	Swift-XRT	00095968001	7.9	98	2126
2021-05-15	Swift-XRT	Merged 1	10.6	157	14
2021-06-15	Swift-XRT	Merged 2	8.2	100	31
2021-08-15	Swift-XRT	00095968008	8.3	110	61
2021-11-15	Swift-XRT	00095968009	8.8	89	92
2022-12-13	NuSTAR	60802020002	22.1	4291	393
2022-12-31	NuSTAR	60802020004	22.7	3982	18
2023-02-01	NuSTAR	60802020006	21.6	3357	32
2023-03-26	NuSTAR	60802020008	22.1	4015	53
2023-06-28	NuSTAR	60802020010	22.0	2791	94

Note. Column (1): Observation date. (2): Observatory. (3): Observation ID. Two of the Swift-XRT observations have been split into multiple observations taken on consecutive days. More specific details on these (including ObsID) can be found in Table 2. Column (4): Net exposure time in units of kiloseconds. For XMM-Newton, we list the pn camera exposure. Column (5): Total counts in the 0.5–7 keV band (for Swift-XRT, XMM-Newton, and Chandra) or in the 3–50 keV band for NuSTAR. Counts from different cameras/modules are summed up. Column (6): Time difference between this observation and the previous observation of the source in days.

Table 2
Swift-XRT-XRT Campaign Observation Details

Set	Date	ObsID	Exp. Time (ks)	Counts	Flux (10^{-13} erg s^{-1})	HR
(1)	(2)	(3)	(4)	(5)	(6)	(7)
1	2021-05-1	00095968001	7.9	98	8.8 ± 1.7	$0.18^{+0.10}_{-0.14}$
2	2021-05-15	00095968002	3.9	48	11.6 ± 3.4	$0.33^{+0.11}_{-0.17}$
	2021-05-17	00095968003	1.9	34	10.9 ± 3.8	$0.23^{+0.15}_{-0.24}$
	2021 May 19	00095968004	4.8	73	9.9 ± 2.2	$0.24^{+0.10}_{-0.14}$
	Merged 1	⋯	10.6	155	11.1 ± 1.8	$0.22^{+0.08}_{-0.10}$
3	2021-06-15	00095968005	3.3	33	6.7 ± 2.5	$0.39^{+0.11}_{-0.21}$
	2021-06-17	00095968006	1.4	24	8.9 ± 4.9	$0.16^{+0.19}_{-0.35}$
	2021-06-19	00095968007	3.5	39	9.7 ± 3.1	$-0.02^{+0.20}_{-0.31}$
	Merged 2	⋯	8.2	96	7.2 ± 1.5	$0.13^{+0.10}_{-0.13}$
4	2021-08-15	00095968008	8.3	110	14.9 ± 1.2	$0.22^{+0.09}_{-0.12}$
5	2021-11-15	00095968009	8.8	89	7.4 ± 1.9	$-0.08^{+0.14}_{-0.19}$

Note. Column (1): Observation group. Column (2): Individual observation date. Column (3): Observation ID. Column (4): Exposure time. Column (5): Total counts in the 0.5–7 keV band. Column (6): Observed flux in the 0.5–7 keV band. (7): Hardness ratio as (H-S)/(H+S), with S being the number counts in the 0.5–2 keV band, and H being the number counts in the 2–7 keV band.

2.3. Chandra Data Analysis

The Chandra data was reduced with the Chandra Interactive Analysis of Observations software (CIAO) v4.14 (A. Fruscione et al. 2006). To extract the source spectra, a circular region of radius 5" was used, centered around the source. For the background, we used an annulus (inner radius 6", outer radius 15") surrounding the source, making sure any additional resolved sources are excluded.

2.4. Swift-XRT Data Analysis

The Swift-XRT data (D. N. Burrows et al. 2005) were reduced using the XRT Data Analysis Software (XRTDAS) v3.6.1. The Calibration Database (CALDB) v20211020 was run to calibrate the event data files through the `xrtpipeline` task. We extracted the source spectra using a circular region with a 20″ radius, while the background was extracted using an annulus (inner radius 30″ and outer radius 60″), placed around the source, making sure to exclude any additional resolved sources. Two of the five observations belonging to the Swift-XRT monitoring campaign were split into three shorter observations, taking place within consecutive days, which are detailed in Table 2. The shorter observations do not have a sufficiently large number of counts to consider them individually for spectral fitting, and thus, we use the "merged" observations for that purpose. To ascertain it is safe to merge the observations (i.e., that no obvious large variability has taken place between them) we measured the flux and hardness ratio (HR = (H-S)/(H+S), where H and S are the number of counts in the 2–7 keV band and the 0.5–2 keV band,

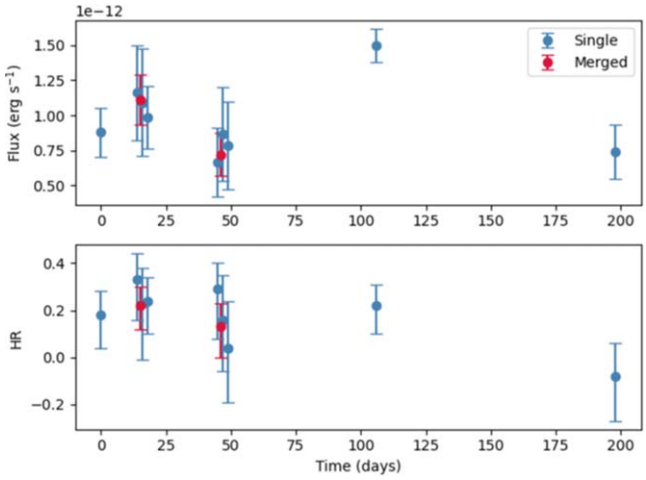

Figure 1. Flux (top) and HR (bottom) as a function of time for the Swift-XRT campaign, showing all observations taken, as described in Table 2. Data groups 2 and 3 are shown as three single observations each (in blue), and as the merged combination of all three (in crimson). Data groups 1, 4, and 5 were originally taken as one single observation, and thus are shown in blue.

respectively). These results are shown in Table 2 and Figure 1. As can be appreciated, no significant changes are taking place within the single observations, and thus, we merge them.

3. X-Ray Spectral Analysis

We fit the source using two recently developed, self-consistent torus models: the broadly used, homogeneous torus model `borus02` (M. Baloković et al. 2018) and the clumpy torus model `UXCLUMPY` (J. Buchner et al. 2019). This choice is consistent with the approach used in previous works by our group (A. Pizzetti et al. 2022; N. Torres-Albà et al. 2023; A. Pizzetti et al. 2025), which used the same models to study $N_{\rm H,los}$ variability in a sample totaling 27 sources so far. Mrk 477 is drawn from the same parent sample, as detailed in Section 1. Using the same models allows us to derive geometric parameters for Mrk 477 that we can compare to the rest of the sample, which are model specific. More specifically, with `borus02` we measure the torus covering factor (C_f), and average torus column density ($N_{\rm H,av}$). With `UXCLUMPY`, we instead derive the width of the Gaussian cloud distribution ($\sigma_{\rm tor}$), and the covering factor of a (possible) additional Compton-thick reflector ($C_{\rm TK}$). Both models, of course, allow us to obtain values of the line-of-sight column density ($N_{\rm H,los}$), which is the objective of this monitoring campaign, as well as values for the inclination angle of the source ($\theta_{\rm obs}$).

The mentioned geometric parameters are derived from the fitting of the reflection component, which is typically assumed to originate in the torus. Because of this, and as already done for the rest of the sample (A. Pizzetti et al. 2022; N. Torres-Albà et al. 2023; A. Pizzetti et al. 2025), we consider that the parameters defining this reflected emission do not change across time. That is, the torus as a whole does not vary its properties significantly on timescales of a few decades. Therefore, we fit all observations together, imposing that all reflection parameters remain tied across observations, but allowing intrinsic luminosity variability as well as $N_{\rm H,los}$ variability across different observations. As done in the mentioned works, we also assume that the photon index, Γ, of the main power-law emission does not vary. We further explore the reliability of these assumptions in Section 4.

The source is fit with the following setup for both torus models:

$$\text{Model} = \text{phabs} * (\text{apec} + \text{zgauss} + C_{\rm norm} * \text{AGNModel}), \quad (1)$$

where `phabs` accounts for Galactic absorption in the line of sight, `apec` accounts for thermal bremsstrahlung emission originated in hot gas within the host galaxy, $C_{\rm norm}$ is a constant that accounts for intrinsic luminosity variability between different observations, and the AGN model setup is defined in Sections 3.1 and 3.2 for `borus02` and `UXCLUMPY`, respectively. An additional emission line component ($kT \sim 0.3$ keV), modeled with `zgauss`, was added to adequately reproduce the soft band (<2 keV) emission.

3.1. `borus02`

`borus02` (M. Baloković et al. 2018) is a uniform torus model, which consists of a cold material reflection component (i.e., reflection from the torus), accounting for both continuum and lines. The geometry of this reflecting material can be changed via a covering factor, C_f ($C_f \in [0.1,1.0]$), and its average column density can be changed via $N_{\rm H,av}$. In "decoupled" configuration, one can disentangle the line-of-sight column density (or obscuration, $N_{\rm H,los}$) from $N_{\rm H,av}$, thus obtaining a first approximation to a clumpy medium. That is, the density through which we look at the source is different from the average density of the material, even if the emission reflected from the torus is modeled with a homogeneous medium. The model also includes an inclination angle of the torus, $\theta_{\rm obs}$ ($\theta_{\rm obs} \in [18°–87°]$). As explained above, we impose that C_f, $N_{\rm H,av}$, and $\theta_{\rm obs}$ do not vary across different observations.

Finally, the model also includes a high-energy cutoff, $E_{\rm cut}$ (which we froze at 300 keV, as per the results of studies on the local obscured AGN population; M. Baloković et al. 2020), and an iron abundance, which we froze at Solar abundance due to our inability to constrain it given the data.

The AGN model setup for `borus02` is as follows:

$$\text{AGN Model} = \text{borus02\_v170323a.fits} + \text{zphabs} * \text{cabs} * \text{cutoffpl} + F_s * \text{cutoffpl}, \quad (2)$$

where the table accounts for the reflected emission as described above, and `zphabs` and `cabs` are photoelectric absorption and Compton scattering away from the line of sight due to obscuring material (affecting the main power law, `cutoffpl`, originating from the corona). F_s is the scattering fraction, usually on the order of a few percent, which accounts for the intrinsic power-law emission of the AGN that interacts elastically with the torus. Figure 2 shows this decomposition applied to one of the spectra fit in this work.

We note that `borus02` has been shown to have a problem in the convolution of the Green functions, which can result in an erroneously generated spectrum at both low and high energies (B. Vander Meulen et al. 2023). At high energies, discrepancies start to be apparent at $E > 40$ keV, and become more significant as energy increases (see Figure 16 in the aforementioned work). We note that the effect of this problem in our work is minimal, given how we only fit the spectra up to ~50 keV, and the errors in the data in the 40–50 keV range are large enough to account for the discrepancy. At low energies, the problem only occurs when not observing through the torus (i.e., $\text{Cos}(\theta_{\rm obs}) \gg 0$), which does not affect this work since the `borus02` tables used are those for $\text{Cos}(\theta_{\rm obs}) = 0$. We also note

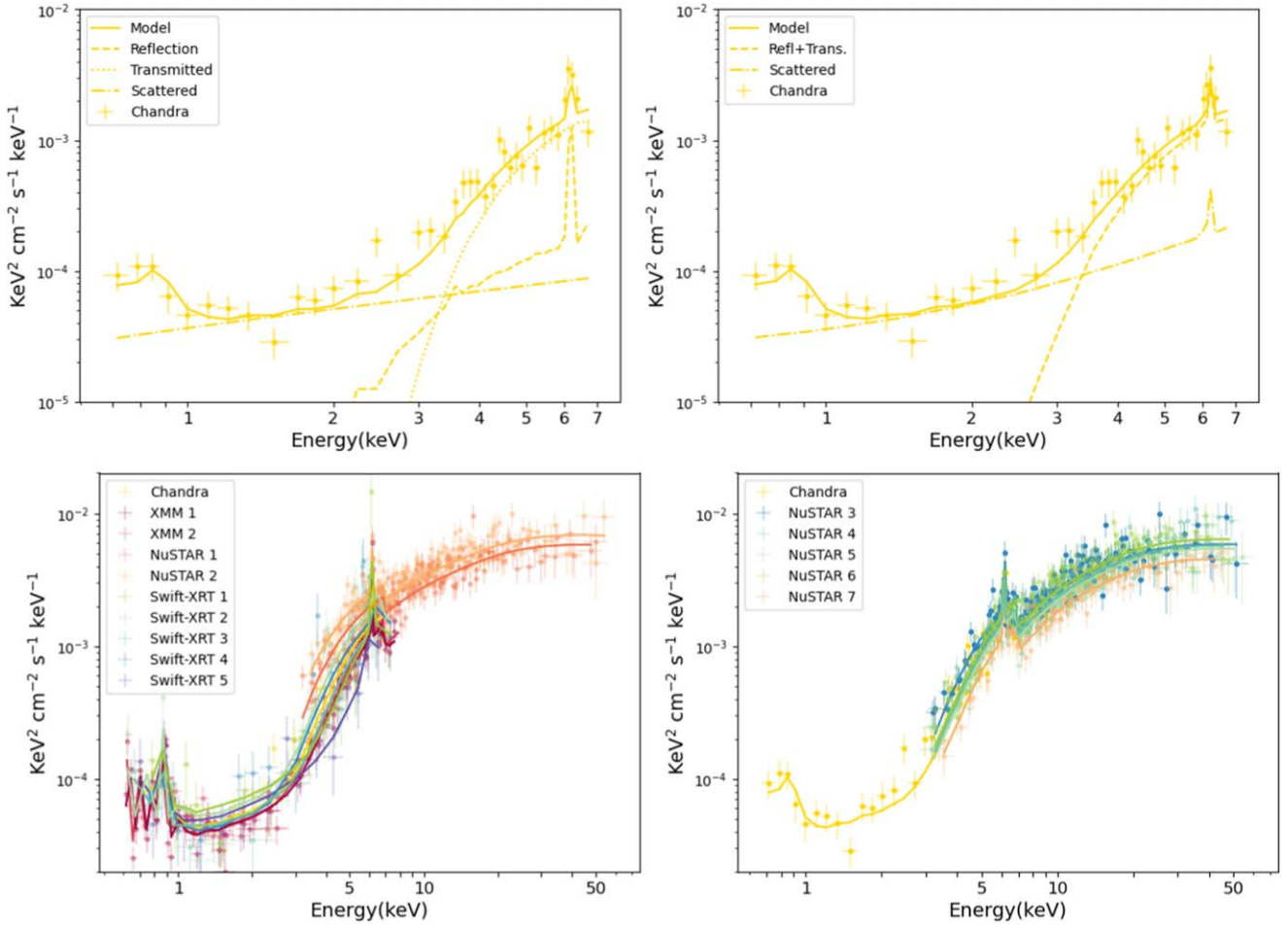

Figure 2. Top: Chandra spectrum of Mrk 477, one of the 15 observations fit simultaneously in this work. Top left: `borus02` fit to the spectrum, showing the subcomponents listed in Equation (2) (reflected, transmitted or line of sight, and scattered emission). Top right: `UXCLUMPY` fit to the spectrum, showing the subcomponents listed in Equation (3) (where the reflected and transmitted components are one single table, with the scattering component added apart). Bottom: all spectra of Mrk 477 used in this work, separated into two panels for display purposes. The Chandra spectrum is shown twice, to serve as a comparison point against the NuSTAR campaign shown on the right plot. The best-fit model using `UXCLUMPY` is shown overlaid on the data with solid lines, to better highlight the spectral variability. All individual spectra and their fit with both `borus02` and `UXCLUMPY` can be found in Appendix A.

that the determination of $N_{\rm H,los}$ by `borus02` has always been in good agreement with both the `UXCLUMPY` and `MYTorus` values in our previous work (S. Marchesi et al. 2019; A. Pizzetti et al. 2022; A. Pizzetti et al. 2025; N. Torres-Albà et al. 2023; D. Sengupta et al. 2024), which now encompasses more than 150 individual observations. As such, our $N_{\rm H,los}$ values are unlikely to be affected by this issue.

However, as they become available, we recommend the usage of alternative torus models (e.g., XCLUMPY, SKIRT, or RXTorusD, A. Tanimoto et al. 2019; B. Vander Meulen et al. 2023; C. Ricci & S. Paltani 2023, respectively), particularly when fitting data up to higher energy ranges.

3.2. *UXCLUMPY*

`UXCLUMPY` is a clumpy torus model (J. Buchner et al. 2019), based on the work of M. Nenkova et al. (2008), which includes a cloud distribution calibrated using known AGN column density distributions (J. Aird et al. 2015; J. Buchner et al. 2015; C. Ricci et al. 2015) and frequencies of observed eclipsing events (A. G. Markowitz et al. 2014). The clouds are set in a Gaussian distribution, above and below the equatorial plane, with a characteristic width $\sigma_{\rm tor}$ ($\sigma_{\rm tor} \in [6^\circ$–$90^\circ]$). This distribution is viewed from a certain inclination angle, $\theta_{\rm obs}$ ($\theta_{\rm obs} \in [0^\circ$–$90^\circ]$).

Unlike `borus02`, the model can be set up using a single component, which accounts for the reflected continuum and lines, as well as the absorbed main power-law emission. Like `borus02`, the model includes a high-energy cutoff, which we again froze to $E_{\rm cut} = 300$ keV.

In addition to the cloud distribution, the model includes a ring of Compton-thick material, which is a necessary addition when fitting sources with particularly strong reflection J. Buchner et al. (2019).[11] This material is characterized by a covering factor, $C_{\rm TK}$ ($C_{\rm TK} \in [0$–$0.6]$), which takes the value of $C_{\rm TK} = 0$ when the source does not require a strong reflection component to explain its spectrum. As explained above, we impose that $C_{\rm TK}$, $\sigma_{\rm tor}$, and $\theta_{\rm obs}$ do not vary across different observations.

The AGN model setup for `UXCLUMPY` is as follows:

$$\text{AGN Model} = \text{uxclumpy.fits} + F_{\rm s} * \text{uxclumpy\_scattered.fits}, \quad (3)$$

[11] See https://github.com/JohannesBuchner/xars/blob/master/doc/uxclumpy.rst for a representation of different possible geometries.

Table 3
Comparison of Common Parameters for the Three Fitting Data Sets: Archival + Swift-XRT, NuSTAR-only, All

	Archival+XRT		NuSTAR-only		Full Data Set	
	borus02	UXCLUMPY	borus02	UXCLUMPY	borus02	UXCLUMPY
kT	$0.29^{+0.06}_{-0.05}$	$0.30^{+0.06}_{-0.05}$	⋯	⋯	$0.29^{+0.07}_{-0.06}$	$0.29^{+0.06}_{-0.05}$
E_{line}	$0.90^{+0.01}_{-0.01}$	$0.91^{+0.01}_{-0.01}$	⋯	⋯	$0.91^{+0.01}_{-0.01}$	$0.91^{+0.01}_{-0.01}$
Γ	$1.54^{+0.05}_{-0.05}$	$1.77^{+0.06}_{-0.05}$	$1.57^{+0.04}_{-0.05}$	$1.80^{+0.03}_{-0.05}$	$1.54^{+0.05}_{-0.06}$	$1.78^{+0.03}_{-0.03}$
$N_{H,av}$	$0.08^{+0.02}_{-0.02}$	⋯	$0.08^{+0.02}_{-0.02}$	⋯	$0.08^{+0.02}_{-0.02}$	⋯
C_f	$1.00^{+u}_{-0.12}$	⋯	1.00^{+u}_{-u}	⋯	$1.00^{+u}_{-0.08}$	⋯
C_{TK}	⋯	0^{*}	⋯	0^{*}	⋯	0^{*}
σ_{tor}	⋯	$84.0^{+u}_{-15.6}$	⋯	$27.8^{+56.2}_{-1.8}$	⋯	$84.0^{+u}_{-7.3}$
Cos (θ_{Obs})	0.05^{+u}_{-u}	0.00^{+u}_{-u}	0.05^{+u}_{-u}	0.00^{+u}_{-u}	0.05^{+u}_{-u}	0.49^{+u}_{-u}
F_s (10^{-2})	$2.46^{+1.23}_{-0.46}$	$18.9^{+2.9}_{-3.2}$	$6.53^{+0.}_{-0.}$	$16.1^{+9.2}_{-1.8}$	$2.80^{+0.83}_{-0.51}$	$20.6^{+1.9}_{-3.3}$
norm (10^{-3})	$1.51^{+0.37}_{-0.54}$	$2.38^{+0.50}_{-0.51}$	$1.62^{+0.19}_{-0.31}$	$3.26^{+0.11}_{-0.25}$	$1.34^{+0.32}_{-0.35}$	$2.14^{+0.35}_{-0.26}$

Note. kT: apec model temperature, in units of keV. E_{line}: Central energy of the added Gaussian line, in units of keV. Γ: power-law photon index. $N_{H,av}$: average torus column density, in units of 10^{24} cm^{-2}. C_f: covering factor of the torus. C_{TK}: covering factor of the additional Compton-thick ring reflector. σ_{tor}: width of the Gaussian cloud distribution. cos (θ_i): cosine of the inclination angle. cos (θ_i) = 1 represents a face-on scenario. F_s: fraction of scattered continuum. Norm: normalization of the AGN emission. (*) Denotes a parameter frozen to the shown value. (⋯) Denotes a parameter that is not included in a given model and/or data set. We note that the NuSTAR-only data set does not include a soft X-ray model, given how the data starts at 3 keV. ($-u$) refers to a parameter being compatible with the hard limit of the available range.

where the first table includes both the line of sight and reflected emission, and F_s is the scattering fraction. UXCLUMPY provides a scattered component with a correction for emission that may leak from the torus after being reflected by the torus at least once. Figure 2 shows this decomposition applied to one of the spectra fit in this work.

4. Results

In this section, we present the results of the fitting process described in Section 3. Table 3 lists the common parameters for all observations (i.e., soft emission parameters, torus parameters, photon index, and scattering fraction), while Table 4 lists the values that are set free to vary for each observation (i.e., $N_{H,los}$, C_{norm}), described in more detail in Section 5.1.

Table 3 shows the results for the best-fit values of the reflection parameters for three different data sets: the archival data plus the Swift-XRT monitoring campaign, the NuSTAR monitoring campaign, and the full data set. This is done for both models, borus02 and UXCLUMPY, with the objective of testing the methodology described in Section 3. That is, the hypothesis that we can assume the reflection parameters do not vary on the timescales considered in this work (∼10 yr). As can be seen in Table 3, there is good agreement between all three data sets (see Appendix B for a more thorough discussion on the viability of this hypothesis).

Despite the strong agreement between the different data sets, the borus02 and UXCLUMPY results present significant differences when it comes to the determination of photon index, Γ. This is a common occurrence when using different torus models (see, e.g., N. Torres-Albà et al. 2023; A. Pizzetti et al. 2025), likely due to the degeneracy between the shape of the reflector (different for each model) and the power-law slope of the incident emission.

As for the rest of the parameters, borus02 favors a high covering factor reflector, but with low obscuring column density ($N_{H,av} \sim 8 \times 10^{22}$ cm^{-2}). This is in agreement with the UXCLUMPY results, for which the covering factor of the thick reflector (C_{TK}) was stuck at the lowest bound, and thus, we froze it to zero.[12] The cloud coverage around the torus, σ_{tor}, is at its highest limit, in accordance with the high covering factor found by borus02. Thus, the models qualitatively agree that the AGN in Mrk 477 is surrounded by a reflector with broad coverage, but low density.

UXCLUMPY does not provide a direct estimate of the average torus column density, but it is possible to estimate the equatorial column density ($N_{H,eq}$), as detailed in A. Pizzetti et al. (2025). The computation of $N_{H,eq}$ depends solely on the values of C_{TK} and σ_{tor}. Using the parameters listed in Table 3, we obtain $N_{H,eq} \sim 6 \times 10^{23}$ cm^{-2}.

The inclination angle is fully unconstrained by both models, and the discrepancy between F_s values is due to the different parameterization of the models, and is a common occurrence for the rest of the parent sample as well (N. Torres-Albà et al. 2023).

Table 4 shows the obscuration for each observation, for the full data set, in two different scenarios: with and without allowing intrinsic flux variability. There are no significant differences between either of these two scenarios or between the two models used, with all agreeing the source varies in $N_{H,los}$ between a few epochs. A more thorough discussion can be found in Section 5.1.

While fit simultaneously, the spectra are shown in two separate plots to avoid overcrowding. Figure 2 (top) shows the borus02 and UXCLUMPY fits, divided into their multiple subcomponents, applied to the Chandra observation alone. The bottom panel shows all spectra used in this work and their best fit with the UXCLUMPY model to highlight the spectral shape diversity. All individual observations, along with their best-fit models with borus02 and UXCLUMPY, can be found in Appendix A (Figures 8 and 9). Given how each spectrum is shown separately, each panel also contains the fit to the Chandra spectrum (as shown in Figure 2) to make it easier to visualize the variability.

[12] As suggested per the model instructions.

Table 4
Mrk 477: Variability Study for the Full Campaign

Model	borus02	UXCLUMPY
Red χ^2	1.00	1.01
χ^2/d.o.f.	1277.7/1272	1286.2/1270
$N_{\rm H,xmm1}$	$0.40^{+0.04}_{-0.04}$	$0.35^{+0.03}_{-0.03}$
$N_{\rm H,xmm2}$	$0.36^{+0.04}_{-0.03}$	$0.32^{+0.03}_{-0.04}$
$N_{\rm H,nus1}$	$0.21^{+0.03}_{-0.03}$	$0.21^{+0.03}_{-0.03}$
$N_{\rm H,nus2}$	$0.17^{+0.02}_{-0.02}$	$0.17^{+0.02}_{-0.03}$
$N_{\rm H,Ch}$	$0.34^{+0.06}_{-0.05}$	$0.28^{+0.04}_{-0.05}$
$N_{\rm H,swift1}$	$0.54^{+0.23}_{-0.15}$	$0.49^{+0.24}_{-0.16}$
$N_{\rm H,swift2}$	$0.30^{+0.09}_{-0.07}$	$0.26^{+0.09}_{-0.06}$
$N_{\rm H,swift3}$	$0.37^{+0.12}_{-0.10}$	$0.33^{+0.15}_{-0.11}$
$N_{\rm H,swift4}$	$0.30^{+0.12}_{-0.08}$	$0.25^{+0.12}_{-0.08}$
$N_{\rm H,swift5}$	$0.75^{+0.55}_{-0.20}$	$0.71^{+0.71}_{-0.25}$
$N_{\rm H,nus3}$	$0.29^{+0.03}_{-0.04}$	$0.27^{+0.03}_{-0.03}$
$N_{\rm H,nus4}$	$0.38^{+0.05}_{-0.04}$	$0.35^{+0.03}_{-0.03}$
$N_{\rm H,nus5}$	$0.34^{+0.06}_{-0.05}$	$0.37^{+0.05}_{-0.04}$
$N_{\rm H,nus6}$	$0.37^{+0.05}_{-0.05}$	$0.35^{+0.04}_{-0.04}$
$N_{\rm H,nus7}$	$0.43^{+0.07}_{-0.06}$	$0.39^{+0.06}_{-0.05}$
$C_{\rm xmm1}$	$0.90^{+0.13}_{-0.11}$	$0.94^{+0.13}_{-0.14}$
$C_{\rm xmm2}$	$0.90^{+0.13}_{-0.11}$	$0.94^{+0.13}_{-0.14}$
$C_{\rm nus1}$	$1.02^{+0.20}_{-0.17}$	$1.13^{+0.30}_{-0.11}$
$C_{\rm nus2}$	$1.15^{+0.22}_{-0.18}$	$1.42^{+0.21}_{-0.24}$
$C_{\rm Ch}$	1^{*}	1^{*}
$C_{\rm swift1}$	$1.32^{+0.40}_{-0.32}$	$1.39^{+0.40}_{-0.35}$
$C_{\rm swift2}$	$1.20^{+0.33}_{-0.25}$	$1.26^{+0.33}_{-0.26}$
$C_{\rm swift3}$	$0.97^{+0.31}_{-0.25}$	$1.02^{+0.32}_{-0.27}$
$C_{\rm swift4}$	$0.97^{+0.35}_{-0.27}$	$1.00^{+0.34}_{-0.26}$
$C_{\rm swift5}$	$1.11^{+0.31}_{-0.24}$	$1.18^{+0.32}_{-0.28}$
$C_{\rm nus3}$	$1.08^{+0.22}_{-0.18}$	$1.27^{+0.19}_{-0.22}$
$C_{\rm nus4}$	$1.13^{+0.26}_{-0.21}$	$1.28^{+0.19}_{-0.22}$
$C_{\rm nus5}$	$1.09^{+0.25}_{-0.20}$	$1.22^{+0.19}_{-0.22}$
$C_{\rm nus6}$	$1.25^{+0.27}_{-0.21}$	$1.42^{+0.21}_{-0.26}$
$N_{\rm H,nus7}$	$0.92^{+0.21}_{-0.17}$	$1.03^{+0.18}_{-0.19}$

Note. Red χ^2 (or Stat): reduced χ^2 or total Statistic. χ^2(or Stat)/d.o.f.: χ^2 (or total Statistic) over degrees of freedom. $N_{\rm H,inst.,num}$: line-of-sight hydrogen column density for a given observation, in units of 10^{24} cm^{-2}. $C_{\rm inst.,num}$: cross-normalization constant for a given observation, with respect to the intrinsic flux of the Chandra observation. (*) Denotes a parameter frozen to the shown value.

5. Discussion

In this section, we discuss the main results of the analysis regarding the variability of $N_{\rm H,los}$ and its characteristics. Section 5.1 discusses obscuration variability for Mrk 477, while Section 5.2 examines the probability of variability for the whole sample of sources analyzed by our group so far. Additionally, Section 5.3 discusses the viability of obscuration variability originating in the BLR. Section 5.4 discusses our results in the context of previous works.

5.1. Obscuration Variability

There are 15 individual observations available for Mrk 477 (see Table 1), which were all used in the "full data set" fit shown in this section. The time span between consecutive observations is as small as 2 days and as large as ∼6 yr. This results in a large variety of timescales (Δt) for which to explore $N_{\rm H,los}$ variability.

Table 4 shows the result of the $N_{\rm H,los}$ variability analysis for the full data set. We consider intrinsic flux variability, which is accounted for through a cross-normalization constant labeled $C_{\rm telescope,number}$, according to the number of observations taken with each telescope in chronological order. All fluxes are normalized to the Chandra observation. The same system is used for the $N_{\rm H,los}$ values listed in both scenarios.

We note that although the vast majority of cross-normalization constants are compatible with 1 (i.e., no intrinsic flux variability) at a 90% confidence level (see Table 4), allowing flux variability still resulted in a better fit. The addition of intrinsic flux variability did not result in large changes in the accompanying $N_{\rm H,los}$ values for each observation, but did imply a slight increase in $N_{\rm H,los}$ errors.

The values of $N_{\rm H,los}$ versus time can be seen in Figure 3 for both models. The figure also includes the cross-normalization variability.

The archival data sets (e.g., the XMM-Newton observations against the second NuSTAR observation) and the monitoring campaigns (e.g., second and last Swift-XRT observations, first and last NuSTAR observations) show $N_{\rm H,los}$ variability. The agreement between borus02 and UXCLUMPY is remarkable, with some minor differences. A few of the $N_{\rm H,los}$ values for UXCLUMPY are slightly lower, while $C_{\rm norm}$ values are higher (and incompatible with 1 at the 90% confidence level). Such differences between combinations of $N_{\rm H,los}$ and $C_{\rm norm}$ between borus02 and UXCLUMPY have been observed before (e.g., N. Torres-Albà et al. 2023; A. Pizzetti et al. 2025), and tend to be more frequent when dealing with NuSTAR data. Looking at the $C_{\rm norm}$ values in Table 4, this is the case in this work as well.

Given the difficulty in visualizing the $N_{\rm H,los}$ variability at all possible timescales, we provide an additional representation. Figures 4 and 5 show 90% confidence contours of $N_{\rm H,los}$ versus $C_{\rm norm}$ for the full data set fit for borus02 and UXCLUMPY, respectively.

For each model, the data is split into two panels, which does not indicate that it corresponds to different data sets being fit separately. Rather, the split is needed in order to avoid overcrowding the plot. To make comparison easier, the scale is kept exactly the same in all four panels. The left panels display the archival data and Swift-XRT campaign, with colors going from dark red to dark blue in chronological order. The right panels start from the last observation shown in the left panels for easier comparison and thus contain the last Swift-XRT observation and the NuSTAR campaign. Since that observation is colored in dark blue, the color order is opposite, and it goes from dark blue to yellow in chronological order. The thick lines connect consecutive observations and go from the best-fit value of one observation into the best-fit value of the next one chronologically. The legend shows the Δt between the two connected observations.

Both borus02 and UXCLUMPY show variability between the same sets of observations. The display chosen in Figures 4 and 5 is particularly useful to see in which timescales there is $N_{\rm H,los}$ variability. In chronological order, there is no variability in $\Delta t = 2$ days between the XMM-Newton observations, given how the contours overlap. There is variability in the 3.8 yr timescale between the XMM-Newton and NuSTAR observations, but again no variability in the shorter $\Delta t = 9$ days between the two archival NuSTAR observations. We note that these two NuSTAR contours do not overlap, but there is a small $N_{\rm H,los}$ range that would overlap when projecting the

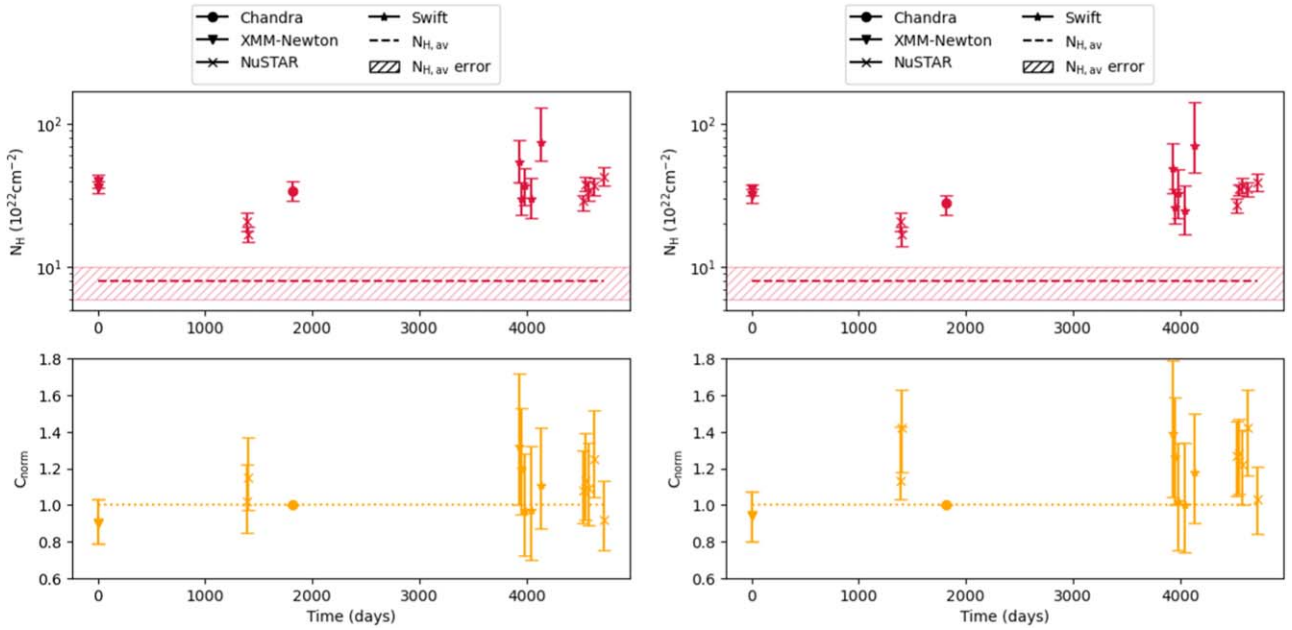

Figure 3. $N_{H,los}$ and C_{norm} variability as a function of time for `borus02` (left) and `UXCLUMPY` (right). The $N_{H,los}$ is compared to $N_{H,av}$ (shaded area) as determined by `borus02` in all panels.

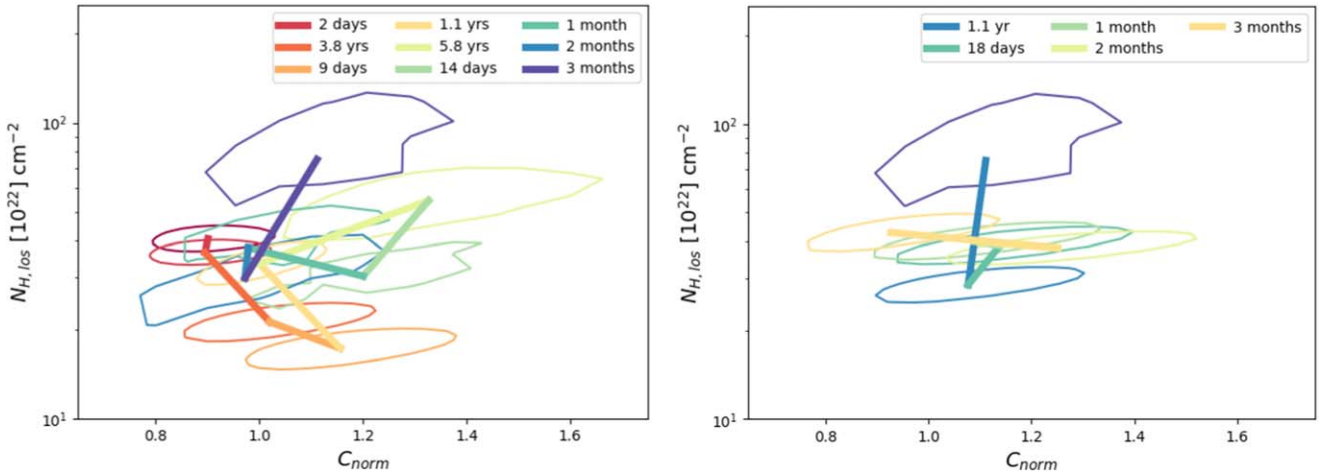

Figure 4. 90% confidence contours of $N_{H,los}$ vs. C_{norm} for the whole data set, as fit by `borus02`. The thick, colored lines go from the best-fit value of one observation to the following observation's best-fit value, in chronological order. The legend shows the Δt between the corresponding consecutive observations. These contours correspond to the full data set shown in Table 4, and have simply been split into two panels to avoid overcrowding the plot. The left panel shows the archival data and Swift-XRT campaign, with observations going from red to dark blue in chronological order. The right panel starts with the last Swift-XRT observation, in dark blue, and goes from dark blue to yellow in chronological order.

contours onto the *y*-axis. Following this logic, we can observe that there is variability in the 1.1 yr timescale, the 5.8 yr timescale (albeit very marginal; the `borus02` contours almost touch), the 14 day timescale between the first two Swift-XRT observations, and the 3 month timescale between the last two Swift-XRT observations. Moving into the right panels, there is variability in the 1.1 yr timescale between the last Swift-XRT observation and the NuSTAR campaign. As for the NuSTAR campaign itself, while there is variability between the first NuSTAR observation and the following four observations, with a minimum timescale of 18 days, the last four observations show no variability.

The variability between different observations can also be appreciated in the spectra shown in the Appendix (Figures 8 and 9), as they are compared to the Chandra spectrum. It is easy to see that, even in the low-quality Swift-XRT observations, the slope in the 2–5 keV range is markedly different between "Swift-XRT 1" and the Chandra spectrum, or "Swift-XRT 5" and the Chandra spectrum.

In summary, Mrk 477 is observed to be $N_{H,los}$ variable over a large range of timescales: years, months, and as little as 14 days. With the data on Mrk 477 alone, it is not possible to determine the most likely timescales of variability. However, Section 5.2 shows that, when adding these data to the rest of the sample, $N_{H,los}$ variability is more likely at longer timescales.

5.2. *Probability of* $N_{H,los}$ *Variability versus Timescale*

Mrk 477 has 15 different observations, which allows us to compare a large number of epochs against each other. The total

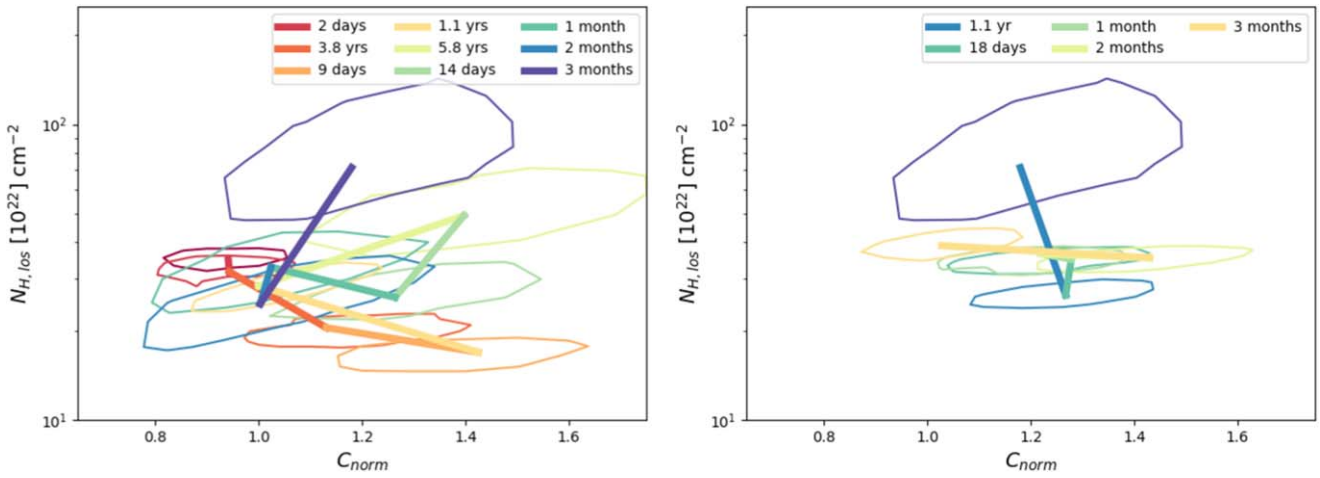

Figure 5. Same as Figure 4 for UXCLUMPY.

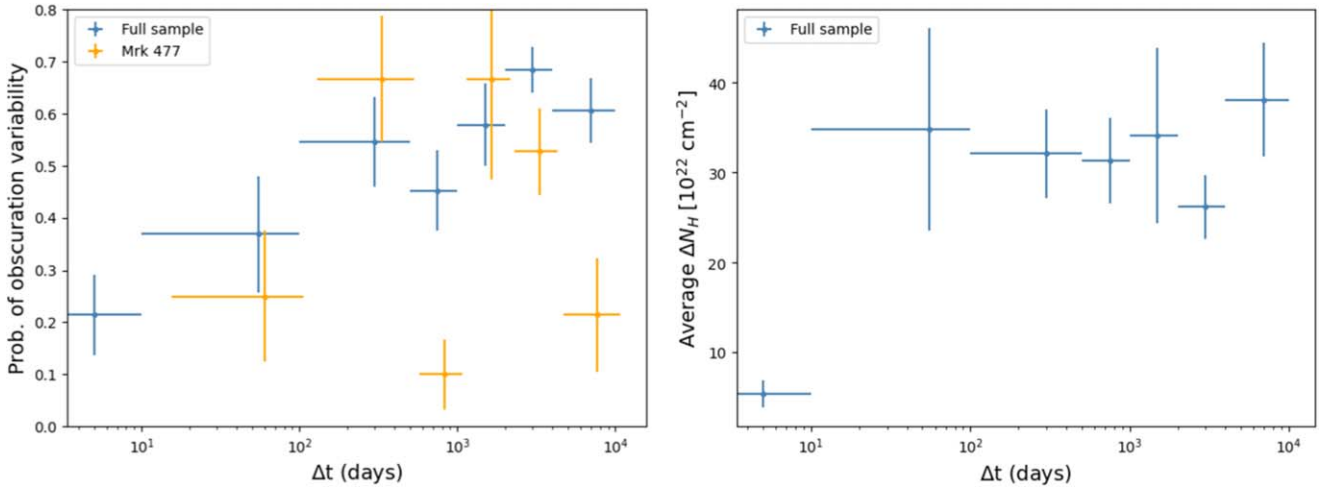

Figure 6. Left: fraction of observation pairs with incompatible $N_{\rm H,los}$ (at 90% confidence) as a function of the time separation between observations. The data shown in blue includes all sources within the parent sample analyzed so far (27 sources, split into A. Pizzetti et al. 2022; N. Torres-Albà et al. 2023; A. Pizzetti et al. 2025; D. Sengupta et al. 2024, and this work). The data shown in orange includes only the observation pairs for Mrk 477. Right: average change in $N_{\rm H,los}$ for all variable observation pairs as a function of the time separation between observations.

number of observation pairs is

$$_{15}C_2 = \sum_{n=0}^{14} n = 105. \quad (4)$$

Out of these, using the values shown in Table 4, we calculate that 42 pairs are $N_{\rm H,los}$ variable. That is, 42 comparisons of one epoch against another are incompatible with having the same $N_{\rm H,los}$ at a 90% confidence level. This results in a probability of finding a variable pair when comparing any two random observations of ∼40%.

Therefore, even if we define Mrk 477 as an "$N_{\rm H,los}$-variable source," the probability of finding it variable using only two observations is <50%. However, the probability of drawing at least one pair of $N_{\rm H,los}$-variable observations grows rapidly with the number of observations taken, being 78% when having three observations (three comparisons) and 95% when having four observations (four comparisons).

With Mrk 477 alone, it is not easy to determine whether this probability is affected by timescales (i.e., the time differences between compared observations). However, when adding the large number of observation pairs for Mrk 477 to the rest of the sample (A. Pizzetti et al. 2022; N. Torres-Albà et al. 2023; A. Pizzetti et al. 2025; D. Sengupta et al. 2024), the total number of pairs available is ∼350. For the first time, we have sufficient statistics to determine the probability of $N_{\rm H,los}$ variability as a function of timescale.

We split the data into bins, such that each bin contains between 30 and 100 observation pairs. The uneven split is due to a much lower number of observations having smaller Δt, which would result in very poor time resolution if split evenly. Within each bin, and for all sources, we calculate the fraction of observation pairs that are incompatible with having the same $N_{\rm H,los}$ at a 90% confidence level. The results are shown in Figure 6. There is a clear trend showing an increased probability of $N_{\rm H,los}$ variability with larger timescales, increasing from ∼20% at $\Delta t < 10$ days to ∼60%–70% at $\Delta t > 2000$ days.

Figure 6 (right) also shows the average $\Delta N_{\rm H,los}$ for all observation pairs in the full sample that present $N_{\rm H,los}$ variability at a 90% confidence level as a function of timescale. The average $\Delta N_{\rm H,los}$ is between 30 and 40 $\times$ 10^{22} cm^{-2} regardless of timescale, with the exception of very short timescales. For $\Delta t < 10$ days, the average variability is much

smaller (5×10^{22} cm^{-2}), with very little variance across all observations. With only six variable pairs, this may be a result of poor statistics, and more data is likely needed to confirm this fact.

Figure 6, however, also shows the probability of finding a variable pair as a function of timescale for Mrk 477 only. As mentioned above, the data for this source contributes a sizable amount of the total observation pairs of the sample (almost a third). As such, it potentially introduces bias into the results. The Mrk 477 data has large spikes in the plot at timescales of ∼2 yr and ∼10 yr, while going to very low probability at timescales of ∼3 yr. This is a result of the uneven sampling brought by the monitoring campaigns, with up to five observations taken very close together (twice) and then a few observations largely separated in time. Since the five observations grouped together tend to have much closer $N_{\rm H,los}$, if one of the lone observations has a different $N_{\rm H,los}$, this counts as five variable pairs at roughly the same timescale of separation. Therefore, our statistical approach is not valid when looking at a single source.

The effect the Mrk 477 has on the trends of the full sample can be perceived by eye, particularly at the timescales mentioned above. While it does not appear to dominate the trend of the full sample, it is worth being aware of its influence. This effect will be minimized as more data is added as a result of increasing the sample size.

5.3. $N_{H,los}$ Variability and BLR Clouds

The origin of obscuration variability in AGN remains generally unknown, mostly due to the lack of constant monitoring in the X-ray regime. As such, the only transits that have a firm, associated origin are those that are short enough to be fully characterized within one single observation. All of these, which happened in timescales <1 day, have been firmly associated with BLR clouds (e.g., M. Elvis et al. 2004; S. Puccetti et al. 2007; R. Maiolino et al. 2010).

Given how the only confirmed origin of obscuration variability is the BLR, one cannot rule out that it is responsible for all obscuration variability, independently of timescale. That is not to say that a BLR cloud transit lasts for a Δt of years, but rather that two independent observations taken a given Δt apart have intercepted completely different BLR clouds. On the other hand, long-timescale variability could simply originate in larger structures (i.e., the torus) that would have longer transit times, even for a cloud/clump of the same size as a BLR cloud, due to lower velocities.

In this section, we explore how easily BLR clouds could explain the behavior observed in Figure 6 (if at all) in order to potentially rule them out as responsible for obscuration variability at all timescales.

For starters, the fact that there is a dependence of the probability of $N_{\rm H,los}$ variability with timescale already suggests that BLR clouds may not be the exclusive origin of such variability. This is because, above Δt larger than a single cloud eclipsing event (i.e., the cloud crossing time, $t_{\rm cross}$), the probability of observing a difference in $N_{\rm H,los}$ should be independent of timescale.[13] As BLR clouds orbit the SMBH at very close distances, one expects a very quick transit in and out of the line of sight (e.g., $t_{\rm cross} \sim 4$ ks $\simeq 1$ hr, as observed by R. Maiolino et al. 2010). This crossing time is much smaller than the timescales of variability discussed here, and thus, one would always observe a different BLR cloud and obtain a completely unrelated $N_{\rm H,los}$ measurement. Therefore, the probability of measuring $N_{\rm H,los}$ variability should be independent of timescale at $\Delta t \gg 1$ hr. That is, for all bins in Figure 6, the probability should not be dependent on timescale, and instead remain constant. As this is not the case, this figure favors the origin of obscuration variability being at torus scales.

However, in order to be conservative, we explore the possibility that $t_{\rm cross}$ could actually be much longer than 1 hr, and perhaps the lack of such detections is because current observations are biased toward detecting quick transits (i.e., only those that can occur within one single observation, which are at most hundreds of kiloseconds, which is a few days).

As already stated above, the probability of detecting variability should remain constant at $\Delta t > t_{\rm cross}$ (if all variability originates in the BLR). Looking at Figure 6, one could consider that the increase of probability with timescale holds up to about $\Delta t \sim$ 300–500 days, and that for larger timescales the probability is compatible with being roughly constant (at an average rate of ∼60%–70%, within errors). In such a scenario, and as described above, the timescale of ∼300–500 days would correspond to the typical crossing time of an individual BLR cloud. If one assumes Keplerian, circular orbits, and a reasonable SMBH mass range ($M_{\rm SMBH} = 10^7$–$10^8\ M_\odot$), it is possible to obtain a rough approximation of the BLR cloud sizes by simply doing

$$v = \sqrt{\frac{GM_{\rm SMBH}}{r}}, \tag{5}$$

where v is the Keplerian velocity, G is the gravitational constant, and r is the distance to the SMBH. The cloud size ($R_{\rm c}$) is then computed as $v = R_{\rm c} \times t_{\rm cross}$.

We also consider that such large clouds cannot exist stably arbitrarily close to the SMBH since its gravitational influence would result in tidal disruption. We use Equation (5) in K. Ichikawa & R. Tazaki (2017) in order to calculate the radius below which clouds would be unstable:

$$R_{\rm c} = 4.8 \times 10^{-3} \left(\frac{c_s}{3\ {\rm km\ s^{-1}}}\right) \left(\frac{r}{1\ {\rm pc}}\right)^{3/2} \left(\frac{M_{\rm SMBH}}{10^8\ M_\odot}\right)^{-1/2}, \tag{6}$$

in units of parsec, where c_s is the speed of sound in the medium, computed as $c_s = \sqrt{k_B T/\mu {\rm m}_p}$. We assume a BLR cloud temperature of roughly $\sim 10^4$ K (see, e.g., D. Ilic et al. 2008), a mean molecular weight $\mu = 0.5$ as is suitable for the ionized gas of the BLR (A. L. Müller et al. 2022), $k_{\rm B}$ is the Boltzmann constant and m_p is the proton mass.

Figure 7 shows the results of this simple calculation for all reasonable cloud distances to the SMBH. The vertical lines show BLR sizes as estimated by the GRAVITY collaboration for 26 AGN (smallest size $R_{\rm BLR} = 2$ lt-days, largest size $R_{\rm BLR} = 150$ lt-days, and average BLR size $R_{\rm BLR} \sim 30$ lt-days, Gravity Collaboration et al. 2023). In all instances, the BLR cloud sizes remain ∼2–3 orders of magnitude larger than previous estimates ($\sim 10^{13}$ cm) (e.g., R. Maiolino et al. 2010; H. Netzer 2015). Moreover, the majority of the area in the plot falls within a region within which the clouds would likely be tidally disrupted. Only for black hole masses $M_{\rm SMBH} \leqslant 10^7 M_\odot$,

[13] Provided the cloud distribution is homogeneous.

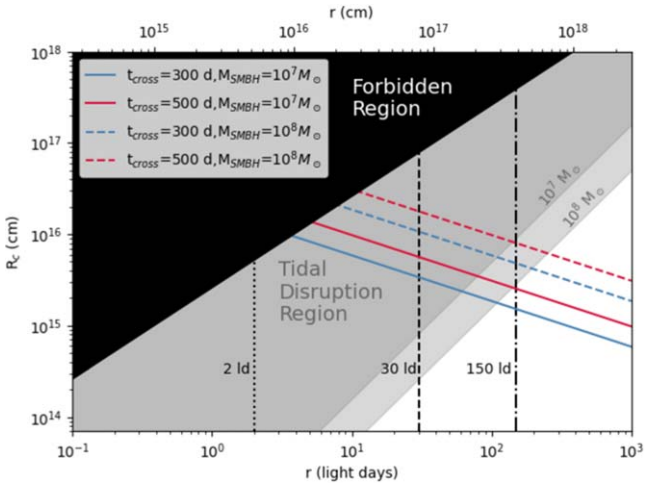

Figure 7. BLR cloud sizes as a function of radial distance, computed under the assumption of two different M_{SMBH} and a cloud crossing time of $t_{cross} = 300$ days (blue) and $t_{cross} = 500$ days (red). The black shaded area corresponds to a "forbidden region," an area removed from the plot as the clouds in it would be larger than their distance to the SMBH. The gray shaded areas correspond to "tidal disruption regions," where clouds would not remain stable due to the gravitational influence of the SMBH. The vertical lines correspond to the minimum, average, and maximum BLR sizes observed by GRAVITY Collaboration et al. (2023).

and if the BLR has an above-average size, clouds this large can stably exist.

The other obvious possible explanation is that BLR clouds are only responsible for variability at much shorter timescales than 300–500 days, after which the torus takes over as the main origin. This hypothesis is supported by Figure 6 (right), which shows a different average $\Delta N_{H,los}$ only at $\Delta t < 10$ days. That is, it could be that obscuration variability at $\Delta t < 10$ days is the only one caused exclusively by BLR clouds, and that their average column density is about 5×10^{22} cm^{-2}. This would align with the results of R. Maiolino et al. (2010), who observed $\Delta N_{H,los} = 5$–10×10^{22} cm^{-2} in the two consecutive eclipses attributed to BLR clouds. Indeed, repeating the calculations shown in Figure 7 with $t_{cross} = 10$ days would lead to a cloud size of $\sim 5 \times 10^{13}$ cm at 150 lt-days, which, again, is much more compatible with previous observations.

However, it is worth mentioning that, using this simplified method, we cannot rule out that a complex cloud distribution (i.e., with cloud density/size depending on the distance to the SMBH) could reproduce the variability pattern in Figure 6. In future works, we will explore the exact BLR properties that could reproduce it (if any).

5.4. Variability Results in the Context of Previous Work

The work presented here uses one of the largest samples to date, if not the largest, when it comes to exploring the typical timescales and values of obscuration variability. As such, comparing the results shown in Figure 6 to previous works is not trivial. Indeed, most works on obscuration variability to date focus on single sources (e.g., A. Pizzetti et al. 2022; A. Kayal et al. 2023). Furthermore, they also tend to focus on extreme sources rather than the bulk of the population, i.e., those known as "changing-look AGN," which transition from obscured to unobscured (Seyfert 1 to Seyfert 2) (see, e.g., L. Titarchuk et al. 2024, for a review), or from Compton thin to Compton thick (across the $N_{H,los} = 10^{24}$ cm^{-2} threshold, e.g., G. Risaliti et al. 2005; S. Bianchi et al. 2009; M. Guainazzi et al. 2012; E. Marchese et al. 2012; G. Miniutti et al. 2014; C. Ricci et al. 2016; S. Marchesi et al. 2022; R. Serafinelli et al. 2023).

As such, the sample selection is markedly different between the results presented here and those obtained in most previous works. In fact, based on the cited works,[14] the average column density variability in changing-look AGN is $\langle N_{H,los} \rangle \sim 7 \times 10^{23}$ cm^{-2}. This is more than twice the average found for our sample, which is not surprising, given that the mentioned works specifically select sources that have large obscuration variability. Similarly, S. Laha et al. (2020) studied a sample of ~ 20 sources, most of which had an average column density of 1–10 $\times 10^{22}$ cm^{-2}. The average column density variability of the analysis performed in their work is $\langle N_{H,los} \rangle < 5 \times 10^{22}$ cm^{-2}.

These comparisons point to the fact that $\Delta N_{H,los}$ is likely dependent on $N_{H,los}$, and somewhat proportional to it. Therefore, our average obscuration column density variability of $\sim 3 \times 10^{23}$ cm^{-2} is valid for sources with typical $N_{H,los}$ values in the $\sim 10^{23}$–10^{24} cm^{-2} range.

Finally, our results showing that the probability of obscuration variability increases with time are in agreement with those of A. G. Markowitz et al. (2014). A. G. Markowitz et al. (2014) observed a total of eight sources for 17 yr, detecting eight individual eclipsing events. While this is a low number, it remains the largest sample to date with fully observed eclipsing events (i.e., ingress to egress). For timescales larger than 10 days, an increase in the probability of eclipses is observed for both type I and type II AGN. Our results, which do not observe full eclipsing events but are based on a much larger sample of sources and number of events, significantly strengthen their findings.

6. Conclusions

In this work, we have analyzed 15 X-ray observations of Mrk 477, taken with four different telescopes, spanning a total of $\sim$13 yr, and with a large variety of time differences between consecutive observations. Here, we summarize our main conclusions:

1. Mrk 477 presents $N_{H,los}$ variability, between multiple sets of observations, and with timescales as short as $\sim$2 weeks and as long as years.
2. Although we define Mrk 477 as an "$N_{H,los}$-variable source," the probability of finding $N_{H,los}$ variability between any two randomly drawn observations is $\sim$40%. We caution that this rough estimate does not take into account the timescales between different observations, and that more data would be needed to give a statistically meaningful number as a function of Δt.
3. When adding the results of this work to those of another 26 sources analyzed by ourselves, we conclude that $N_{H,los}$ variability is more likely to occur at yearly timescales than at shorter ones ($\sim$days/weeks). The probability of observing a variable pair increases from $\sim$20% at

[14] This includes a comparison between all observation pairs that are incompatible in $N_{H,los}$, within errors in S. Bianchi et al. (2009); E. Marchese et al. (2012); G. Miniutti et al. (2014); C. Ricci et al. (2016); and S. Marchesi et al. (2022). Other works did not present a comprehensive list of $N_{H,los}$ values for all observations of the source, and were thus excluded from this calculation.

$\Delta t < 10$ days, to $\sim$60%−70% at timescales larger than 5 yr.

4. The average $\Delta N_{\rm H,los}$ between variable observations is 30–40 $\times$ 10^{22} cm^{-2} regardless of timescale, with the exception of $\Delta t < 10$ days, for which we find an average variation of 5 $\times$ 10^{22} cm^{-2}.
5. Mrk 477 is best described as a thin reflector with a large covering factor by `borus02`. `UXCLUMPY` qualitatively agrees with this description, given how it does not require a Compton-thick reflector, and $\sigma_{\rm tor}$ is at the highest possible value.
6. We test the hypothesis of BLR clouds resulting in all of the observed $N_{\rm H,los}$ variability, for all sources. If we assume a homogeneous cloud distribution, we can easily attribute $N_{\rm H,los}$ variability to BLR clouds at timescales of $\Delta t < 10$ days. On the other hand, under the same hypothesis, BLR clouds would need to have sizes $>10^{15}$ cm to explain variability at larger timescales. This is 2 orders of magnitude larger than previously observed/assumed. However, we cannot rule out that a particular distribution of cloud sizes and density as a function of radial distance to the SMBH could reproduce the data.
7. Mrk 477 shows no variability in reflection parameters (that is, geometrical parameters of the torus, such as C_f, $N_{\rm H,av}$, and $\sigma_{\rm tor}$) when splitting the full observation data set into two subsets. The same is true for the photon index.

Acknowledgments

We thank the referee for the useful comments and suggestions. N.T.A., M.A., and I.C. acknowledge funding from NASA under contracts 80NSSC23K1611, 80NSSC23K0484, and 80NSSC23K0484. The scientific results reported in this article are based on observations made by the X-ray observatories NuSTAR, XMM-Newton, Chandra, and Swift-XRT, and has made use of the NASA/IPAC Extragalactic Database (NED), which is operated by the Jet Propulsion Laboratory, California Institute of Technology under contract with NASA. We acknowledge the use of the software packages XMM-SAS and HEASoft.

Appendix A
Individual Spectra

In this appendix, we present spectra for each individual observation, fit with both `borus02` and `UXCLUMPY`, in Figures 8 and 9, respectively. All spectra were fit simultaneously, but we opt to show them separately in order to avoid overcrowding the plot. For easier comparison, and in order to appreciate the time variability, all spectra are compared to the same Chandra best fit, as shown in Figure 2. The colors used to plot the spectra match, observation-wise, the contours in Figures 4 and 5. The spectra are displayed in chronological order.

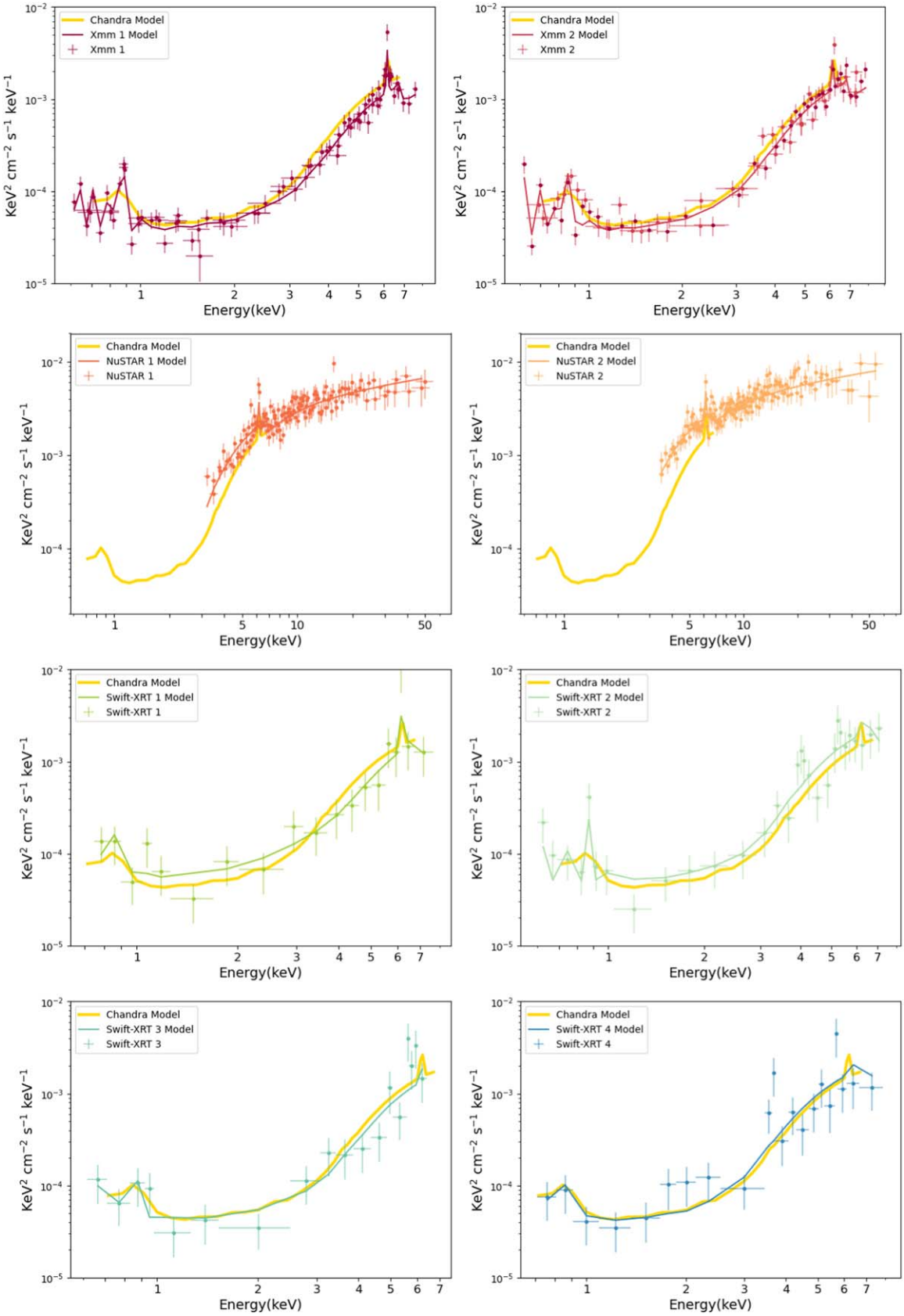

Figure 8. All observations used in this work, except for the Chandra observation already shown in Figure 2, as fit with `borus02`. They are individually compared to the reference Chandra observation. The spectra are shown in chronological order.

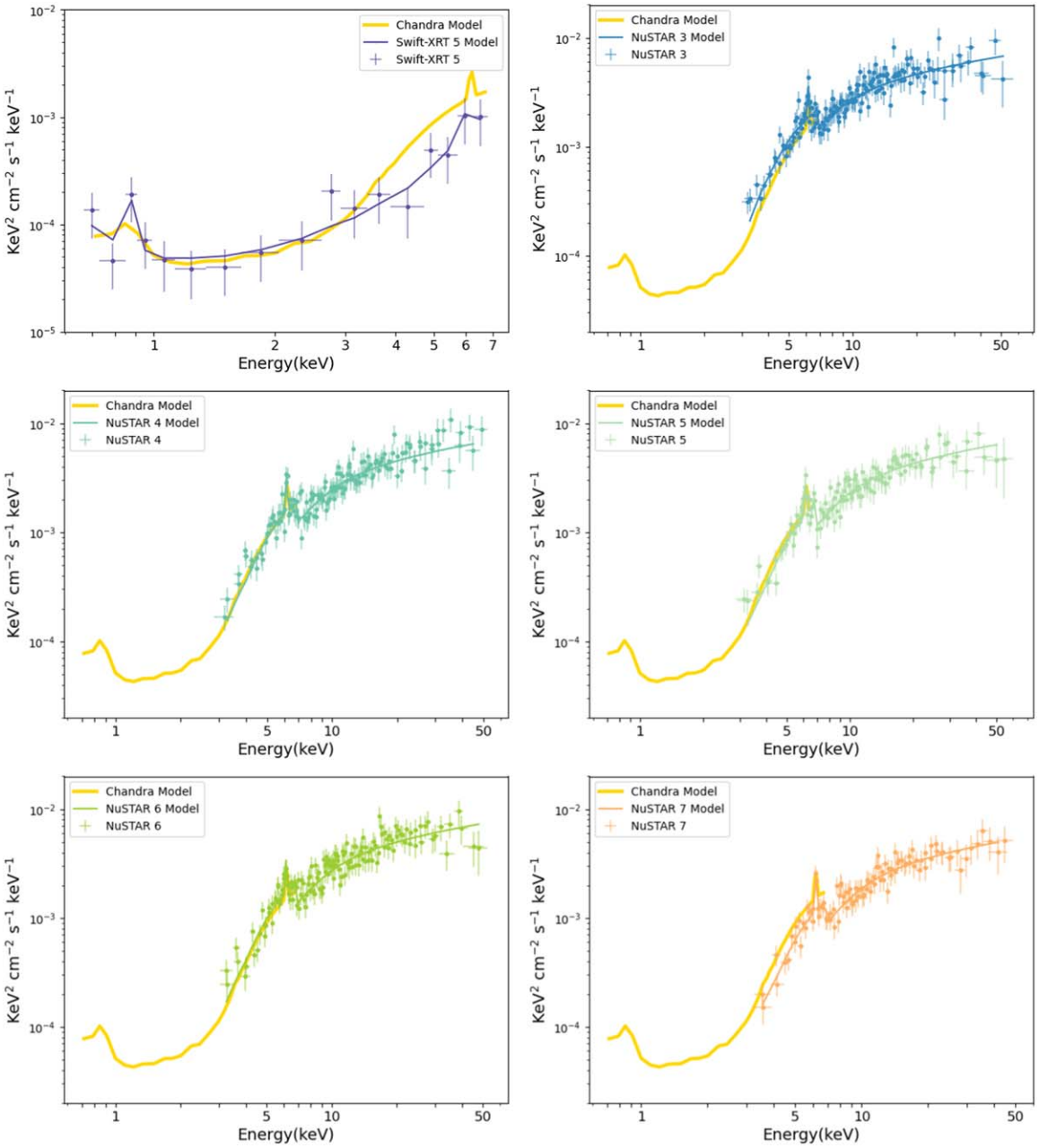

Figure 8. (Continued.)

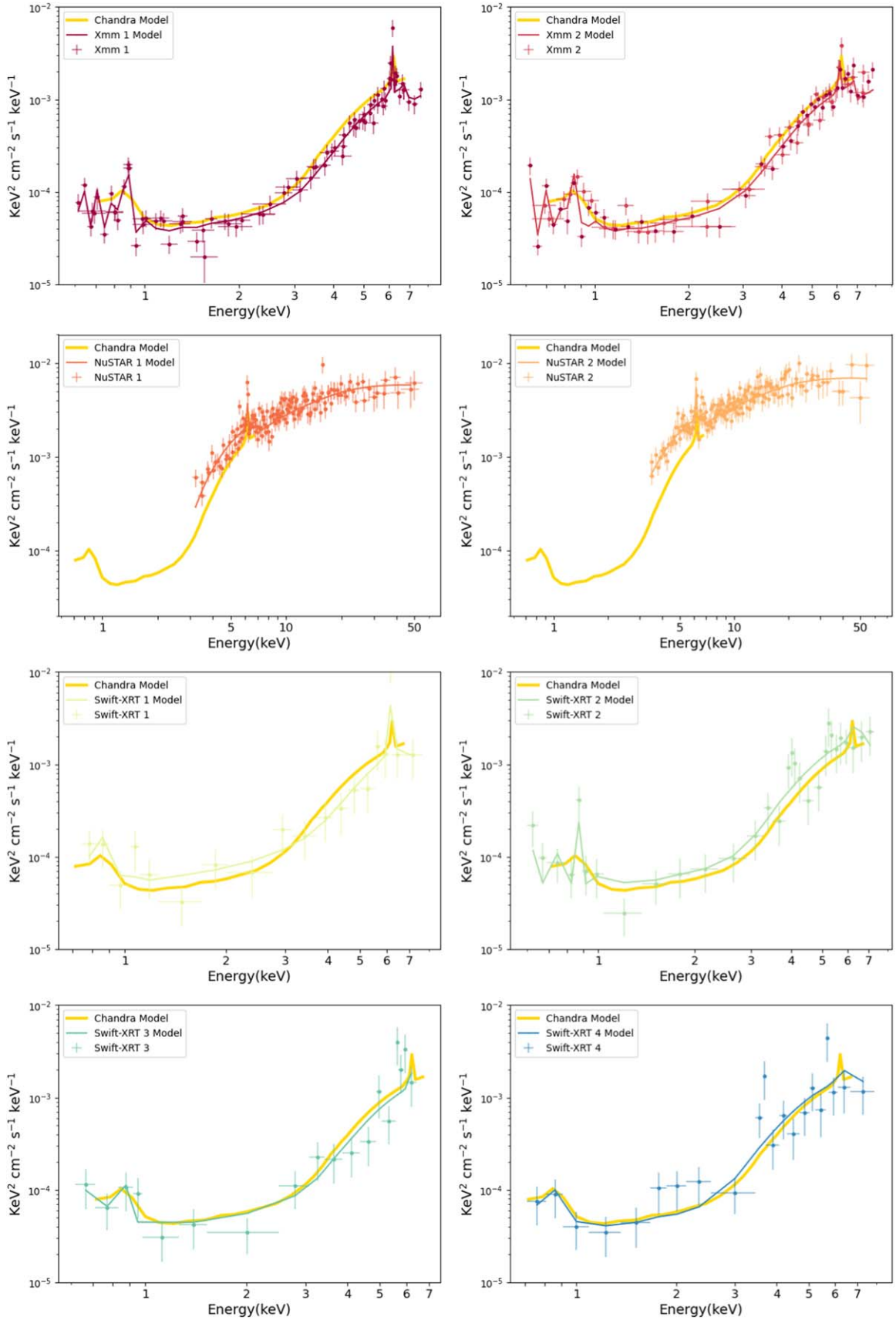

Figure 9. All observations used in this work, except for the Chandra observation already shown in Figure 2, as fit with UXCLUMPY. They are individually compared to the reference Chandra observation. The spectra are shown in chronological order.

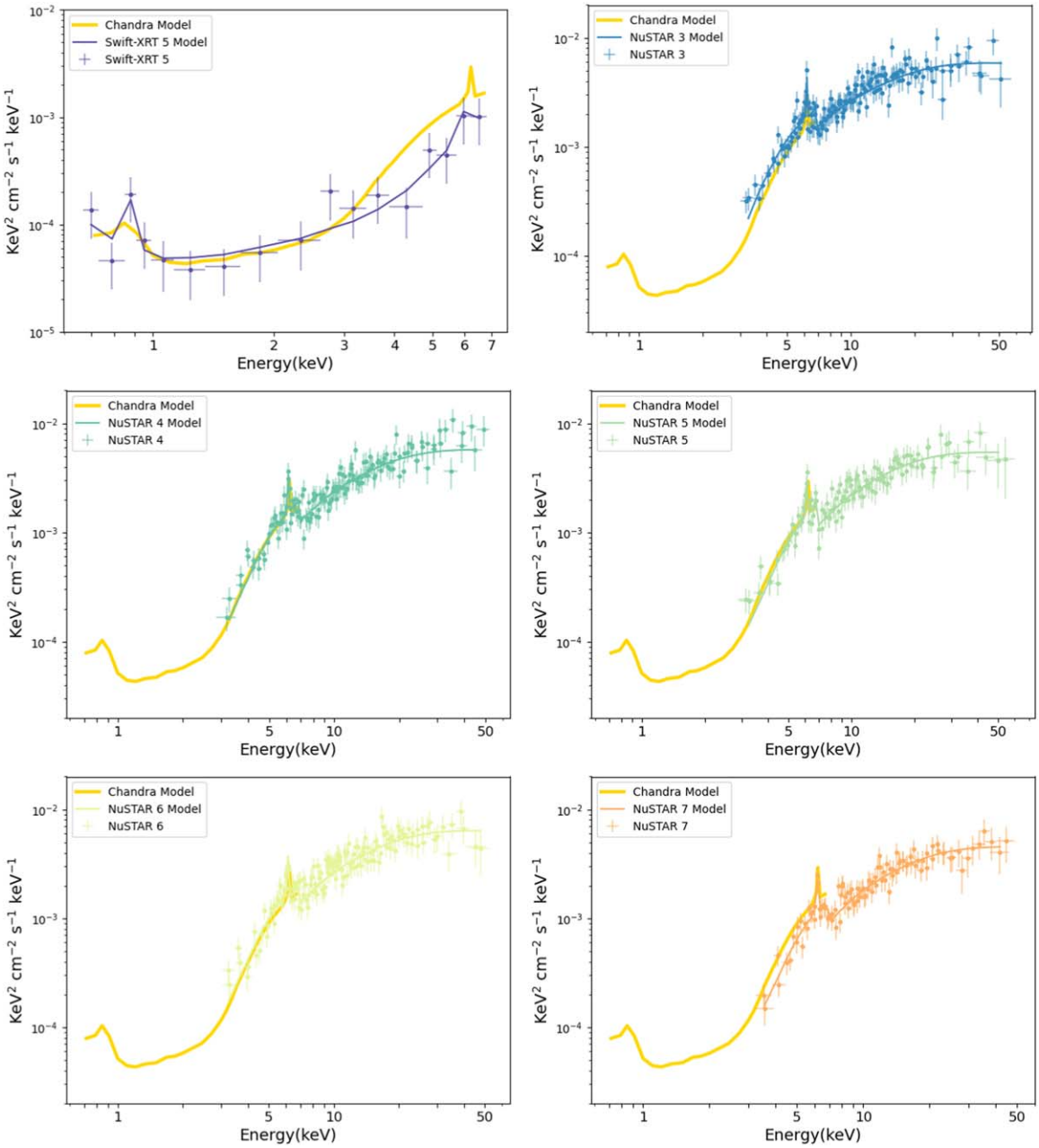

Figure 9. (Continued.)

Appendix B
Nonvariability of the Torus Geometry

One of the fundamental assumptions of the fitting process described in this work, as well as in the analysis of the parent sample in A. Pizzetti et al. (2022), N. Torres-Albà et al. (2023), and A. Pizzetti et al. (2025), is that one can consider that the reflection parameters do not change in timescales of ∼10–20 yr. This is a necessary assumption when dealing with monitoring campaigns that do not have simultaneous soft (<10 keV) and hard (>10 keV) coverage, or with archival data.[15] Indeed, the full band is needed to constrain parameter degeneracies and separate $N_{\rm H,av}$ variability from intrinsic luminosity variability.[16]

With the modeling described in this work, as well as in the aforementioned works, it is possible to break the degeneracy because full band coverage is available, even if not simultaneous. That is, under the assumption of nonvariability of the reflector. However, a few bright and well-known sources are known to show reflection variability in similar timescales (see, e.g., P. G. Boorman et al. 2024, and references therein). It is currently unknown how common this phenomenon is, although it is certain that it would require the reflector to have a scale much smaller than the scales of the torus (≪1–10 pc) to

[15] This is the vast majority of observations for AGN in X-rays, with only about ∼10% of NuSTAR time having simultaneous observations with either Chandra, Swift-XRT, or XMM-Newton (see Figure 6 in P. G. Boorman et al. 2024).

[16] And even under the mentioned assumption, it is sometimes impossible to disentangle between the two; see N. Torres-Albà et al. (2023) and A. Pizzetti et al. (2025).

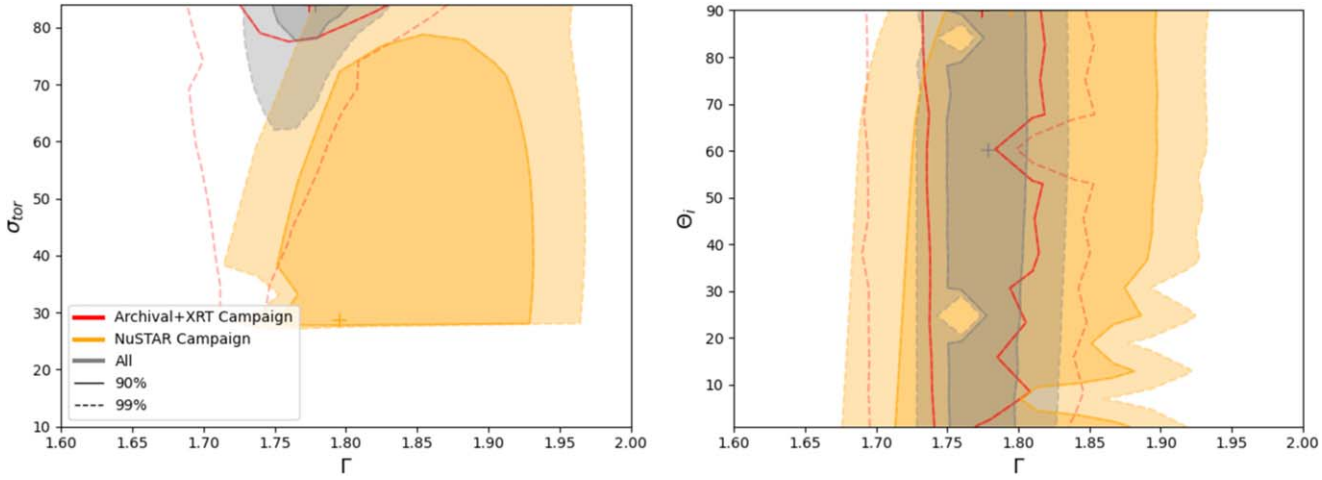

Figure 10. Confidence contours (at 1σ, 2σ, and 3σ) for the width of the torus cloud distribution (left), and inclination angle (right), against the photon index, for the UXCLUMPY model. The different colors represent the different data sets used to test the hypothesis that the reflection parameters do not change: the archival data + Swift-XRT campaign (red), the NuSTAR campaign (blue), and the full data set (green). The colored crosses indicate the best fit. The three data sets are in good agreement, with the parameter determination becoming more tightly constrained when using the full data set.

greatly vary in the observed short timescales. The current, most common assumption in the literature is that reflection occurs all throughout the torus, and in such a case, the nonvariability assumption is valid.

This is not easy to test for the large majority of sources in the archive, given how good quality NuSTAR observations are needed in multiple, different epochs (e.g., P. G. Boorman et al. 2024). Furthermore, a large number of observations at each epoch (or great data quality) may also be needed in order to break degeneracies and reduce errors of the derived parameters (see, e.g., S. Marchesi et al. 2022) to allow for a comparison.

In this work, we are putting together archival observations as well as two different monitoring campaigns. Thanks to the large amount of data, we can test the validity of this hypothesis for Mrk 477, and for this specific data set. Due to data quality and limited band coverage, the Swift-XRT campaign cannot be used to constrain reflection parameters on its own. Therefore, we have split the analysis into two data sets that have a similar total number of counts: the archival data + the Swift-XRT campaign, and the NuSTAR campaign alone. Both sets contain NuSTAR observations, which are key to estimating reflection parameters.

Table 3 contains the results for the parameters considered to be common among all observations for three different fits: the two separate data sets mentioned above, and the full data set. For the purposes of this comparison, we only show the common parameters in Table 3, but the result of the full fit (for the split data sets) can be found in Appendix C. The determinations for the parameters that vary in each observation for the full data set fit can be found in Section 5.1.

Figures 10 and 11 show contour plots at 90% and 99% confidence levels of the photon index Γ against each of the reflection parameters for UXCLUMPY and borus02, respectively. Both the table and figures show remarkable agreement between the parameter contours of the two data sets and of the full data set.

For the UXCLUMPY model, the parameter that dictates the spread of the cloud distribution ($\sigma_{\rm tor}$) has a different "best-fit" value in the NuSTAR-only campaign fit, with large errors. This is likely due to the fact that the reflector in Mrk 477 is subdominant, and thus difficult to constrain. However, the NuSTAR-only campaign agrees with the other two data sets within the 99% confidence level. It can also be seen how the increase in the number of observations results in much tighter constraints, favoring a higher value of $\sigma_{\rm tor}$, close to the upper limit of $\sigma_{\rm tor} = 84$. The inclination angle is completely unconstrained, which is not uncommon, even for large data sets with multiple observations (see, e.g., N. Torres-Albà et al. 2021; A. Pizzetti et al. 2025). The contours become narrower for the full data set, which is only a reflection of the tighter constraints on the photon index (Γ).

For the borus02 model we see similar results, with the inclination angle being once more completely unconstrained. The determinations for $N_{\rm H,av}$ are in very good agreement, with a small tightening of the contours as the whole data set is used. The contours for the covering factor show a good agreement around the best-fit value ($C_f = 1$), while also showcasing a complex parameter space, particularly for the NuSTAR-only campaign. As more data is added, these other areas of low $\Delta\chi^2$ are reduced, even if not completely eliminated.

Mrk 477 does not have a dominant reflector (as indicated by the very low $N_{\rm H,av}$ of the borus02 model, and as shown in Figure 2). This fact makes it additionally difficult to constrain some of the reflection parameters despite the abundance of data.

Overall, the agreement between data sets is good. This means that the data is compatible with the reflection parameters and does not vary across observations. It is worth noting that since the reflection parameters are mostly fit through the NuSTAR observations, the test performed compares the torus parameters in 2014 (date of the archival NuSTAR data) versus 2022 (date of the monitoring campaign by NuSTAR). Therefore, the reflection parameters are consistent in a timescale of about a decade.

However, this is not to be taken as definitive proof that the reflector of Mrk 477 is nonvariable, or further extrapolating that, since it is not variable, the reflection originates in the whole torus. Rather, this just serves as a consistency test of our

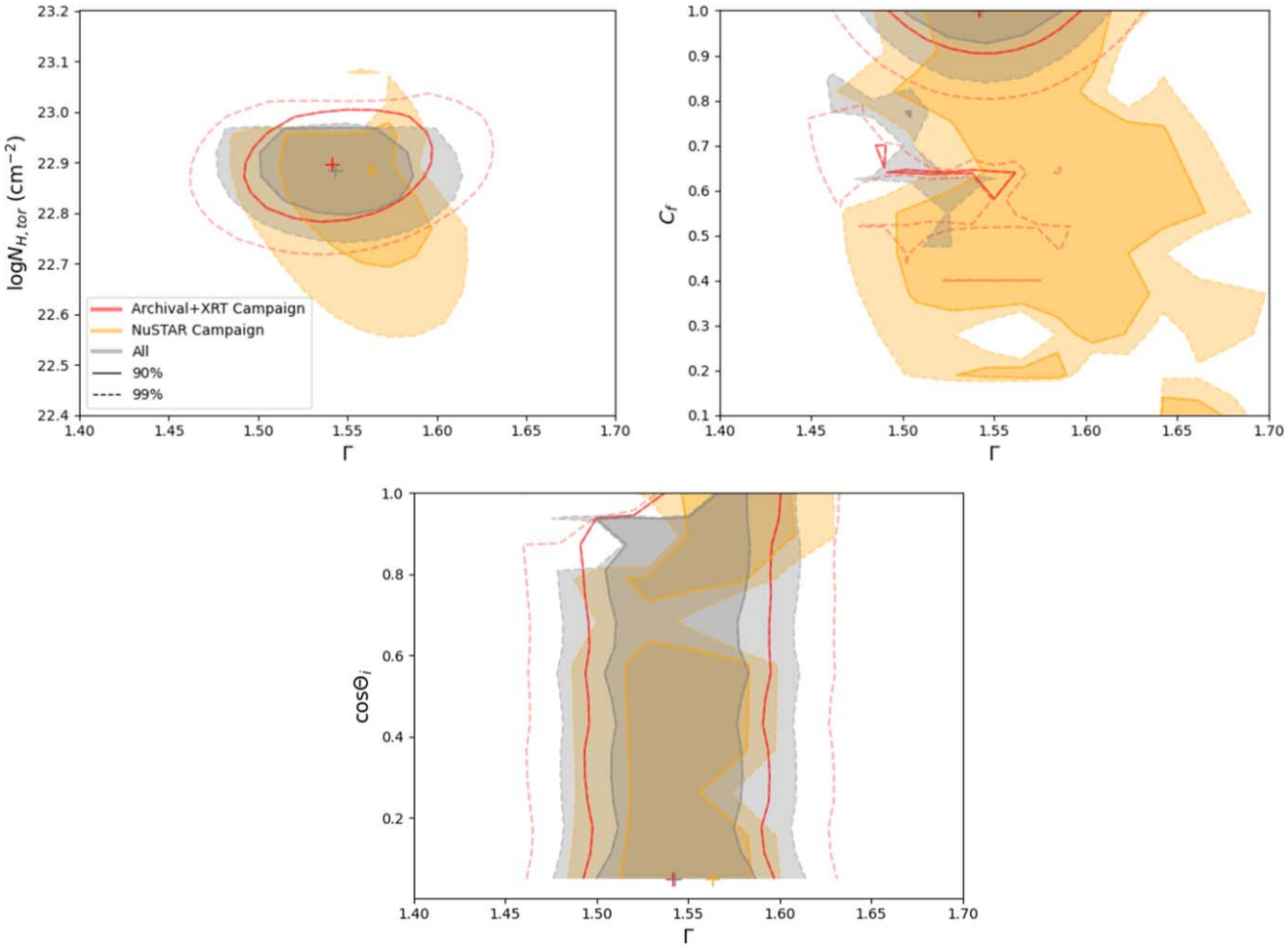

Figure 11. Confidence contours (at 1σ, 2σ, and 3σ) for the width of the cloud distribution (top left), covering factor (top right), and inclination angle (bottom), against the photon index, for the `borus02` model. The different colors represent the different data sets used to test the hypothesis that the reflection parameters do not change: the archival data + Swift-XRT campaign (red), the NuSTAR campaign (blue), and the full data set (green). The colored crosses indicate the best fit. The three data sets are in good agreement, with the parameter determination becoming more tightly constrained when using the full data set.

assumed hypothesis (i.e., that we can impose nonvariability of the reflection parameters for this particular work). In order to fully test this assumption and its physical implications, we would ideally need monitoring campaigns spread over different years, providing high-quality data in both the soft and hard bands, such that it is possible to tightly constrain the reflection parameters in each epoch. Further testing would also require a sizable sample of sources, to determine how common reflection variability is over nonvariability. Sources with a higher reflection dominance would also serve as a better testing benchmark compared to Mrk 477.

Appendix C
Model Tables

Table 3 shows a comparison between the joint fit of all the data and the joint fit of two subsets in terms of the parameters kept constant at all epochs. In this section, we present tables including all of the parameters (kept constant and variable) in the two subsets used for the mentioned comparison: Table 5 shows the full fit for the archival plus Swift-XRT campaign, while Table 6 shows the same for the NuSTAR-only data set. The information added is thus equivalent to that shown in Table 4 for the full data set.

Table 5
Best-fit Parameters for the Archival Data and Swift-XRT Campaign of Mrk 477

Model	borus02	UXCLUMPY
Red χ^2	1.04	1.06
χ^2/d.o.f.	622.5/596	629.9/596
kT	$0.29^{+0.06}_{-0.05}$	$0.30^{+0.06}_{-0.05}$
E_{line}	$^{+0.01}_{-0.01}$	$0.91^{+0.01}_{-0.01}$
Γ	$1.54^{+0.05}_{-0.05}$	$1.77^{+0.06}_{-0.05}$
$N_{H,av}$	$0.08^{+0.02}_{-0.02}$	...
C_f	$1.00^{+u}_{-0.12}$	...
C_{TK}	...	0^*
σ_{tor}	...	$84.0^{+u}_{-15.6}$
Cos (θ_{Obs})	0.05^{+u}_{-u}	0.00^{+u}_{-u}
F_s (10^{-2})	$2.46^{+1.23}_{-0.46}$	$18.9^{+2.9}_{-3.2}$
norm (10^{-3})	$1.51^{+0.37}_{-0.54}$	$2.38^{+0.50}_{-0.51}$
$N_{H,Ch}$	$0.38^{+0.05}_{-0.05}$	$0.30^{+0.05}_{-0.07}$
$N_{H,xmm1}$	$0.44^{+0.04}_{-0.04}$	$0.37^{+0.04}_{-0.04}$
$N_{H,xmm2}$	$0.40^{+0.03}_{-0.03}$	$0.33^{+0.03}_{-0.04}$
$N_{H,nus1}$	$0.21^{+0.03}_{-0.03}$	$0.19^{+0.04}_{-0.03}$
$N_{H,nus2}$	$0.17^{+0.02}_{-0.02}$	$0.16^{+0.03}_{-0.03}$
$N_{H,swift1}$	$0.60^{+0.19}_{-0.13}$	$0.53^{+0.24}_{-0.17}$
$N_{H,swift2}$	$0.33^{+0.08}_{-0.06}$	$0.27^{+0.09}_{-0.06}$
$N_{H,swift3}$	$0.41^{+0.12}_{-0.10}$	$0.35^{+0.16}_{-0.11}$
$N_{H,swift4}$	$0.33^{+0.12}_{-0.08}$	$0.25^{+0.12}_{-0.08}$
$N_{H,swift5}$	$0.82^{+0.55}_{-0.20}$	$0.75^{+0.79}_{-0.25}$
C_{Ch}	1^*	1^*
C_{xmm1}	$0.89^{+0.14}_{-0.11}$	$0.90^{+0.17}_{-0.11}$
C_{xmm2}	$0.88^{+0.14}_{-0.11}$	$0.91^{+0.16}_{-0.11}$
C_{nus1}	$0.90^{+0.21}_{-0.14}$	$1.08^{+0.17}_{-0.11}$
C_{nus2}	$1.02^{+0.23}_{-0.16}$	$1.26^{+0.31}_{-0.19}$
C_{swift1}	$1.31^{+0.40}_{-0.31}$	$1.34^{+0.38}_{-0.35}$
C_{swift2}	$1.18^{+0.33}_{-0.25}$	$1.19^{+0.30}_{-0.26}$
C_{swift3}	$0.96^{+0.31}_{-0.24}$	$0.98^{+0.29}_{-0.27}$
C_{swift4}	$0.96^{+0.37}_{-0.27}$	$0.96^{+0.33}_{-0.25}$
C_{swift5}	$1.09^{+0.31}_{-0.24}$	$1.13^{+0.30}_{-0.27}$

Note. Refer to Tables 3 and 4 for notes on parameter definitions and symbols.

Table 6
Best-fit Parameters for the NuSTAR-only Campaign of Mrk 477

Model	borus02	UXCLUMPY
Red χ^2	0.94	0.94
χ^2/d.o.f.	631.4/673	637.3/681
Γ	$1.57^{+0.03}_{-0.06}$	$1.80^{+0.03}_{-0.05}$
$N_{H,av}$	$0.08^{+0.02}_{-0.02}$	...
CF (Tor)	1.00^{+u}_{-u}	...
CTKcover	...	0^*
σ_{tor}	...	$27.8^{56.2}_{-1.8}$
Cos (θ_{Obs})	0.05^{+u}_{-u}	0.00^{+u}_{-u}
F_s (10^{-2})	$6.53^{+0.86}_{-0.15}$	$16.1^{+9.2}_{-1.8}$
norm (10^{-3})	$1.62^{+0.19}_{-0.31}$	$3.26^{+0.11}_{-0.25}$
$N_{H,nus1}$	$0.38^{+0.05}_{-0.05}$	$0.34^{+0.05}_{-0.04}$
$N_{H,nus2}$	$0.48^{+0.10}_{-0.02}$	$0.46^{+0.02}_{-0.03}$
$N_{H,nus3}$	$0.50^{+0.10}_{-0.03}$	$0.47^{+0.03}_{-0.03}$
$N_{H,nus4}$	$0.48^{+0.05}_{-0.02}$	$0.43^{+0.02}_{-0.02}$
$N_{H,nus5}$	$0.51^{+0.08}_{-0.03}$	$0.48^{+0.03}_{-0.04}$
C_{nus1}	1^*	1^*
$C_{H,nus2}$	$1.07^{+0.03}_{-0.09}$	$1.04^{+0.10}_{-0.04}$
$C_{H,nus3}$	$1.04^{+0.04}_{-0.10}$	$1.00^{+0.10}_{-0.03}$
$C_{H,nus4}$	$1.20^{+0.04}_{-0.15}$	$1.13^{+0.03}_{-0.10}$
$C_{H,nus5}$	$0.85^{+0.09}_{-0.03}$	$0.82^{+0.31}_{-0.19}$

Note. Refer to Tables 3 and 4 for notes on parameter definitions and symbols.

ORCID iDs

N. Torres-Albà https://orcid.org/0000-0003-3638-8943
Z. Hu https://orcid.org/0009-0009-3413-5919
I. Cox https://orcid.org/0000-0003-2287-0325
S. Marchesi https://orcid.org/0000-0001-5544-0749
M. Ajello https://orcid.org/0000-0002-6584-1703
A. Pizzetti https://orcid.org/0000-0001-6412-2312
I. Pal https://orcid.org/0000-0002-7825-1526
R. Silver https://orcid.org/0000-0001-6564-0517
X. Zhao https://orcid.org/0000-0002-7791-3671

References

Aird, J., Coil, A. L., Georgakakis, A., et al. 2015, MNRAS, 451, 1892
Anders, E., & Grevesse, N. 1989, GeCoA, 53, 197
Arnaud, K. A. 1996, in ASP Conf. Ser. 101, Astronomical Data Analysis Software and Systems V, ed. G. H. Jacoby & J. Barnes (San Francisco, CA: ASP), 17
Baloković, M., Brightman, M., Harrison, F. A., et al. 2018, ApJ, 854, 42
Baloković, M., Harrison, F. A., Madejski, G., et al. 2020, ApJ, 905, 41
Bianchi, S., Piconcelli, E., Chiaberge, M., et al. 2009, ApJ, 695, 781
Boorman, P. G., Torres-Albà, N., Annuar, A., et al. 2024, FrASS, 11, 1335459
Buchner, J., Brightman, M., Nandra, K., Nikutta, R., & Bauer, F. E. 2019, A&A, 629, A16
Buchner, J., Georgakakis, A., Nandra, K., et al. 2015, ApJ, 802, 89
Burrows, D. N., Hill, J. E., Nousek, J. A., et al. 2005, SSRv, 120, 165
Cox, I. S., Torres-Albà, N., Marchesi, S., et al. 2023, ApJ, 958, 155
Elvis, M., Risaliti, G., Nicastro, F., et al. 2004, ApJL, 615, L25
Fruscione, A., McDowell, J. C., Allen, G. E., et al. 2006, Proc. SPIE, 6270, 62701V
Gravity Collaboration, Amorim, A., Bourdarot, G., et al. 2023, A&A, 669, A14
Guainazzi, M., La Parola, V., Miniutti, G., Segreto, A., & Longinotti, A. L. 2012, A&A, 547, A31
Harrison, F. A., Craig, W. W., Christensen, F. E., et al. 2013, ApJ, 770, 103
Heckman, T. M., González-Delgado, R., Leitherer, C., et al. 1997, ApJ, 482, 114
Hernández-Garcìa, L., Masegosa, J., González-Martìn, O., & Márquez, I. 2015, A&A, 579, A90
Ichikawa, K., & Tazaki, R. 2017, ApJ, 844, 21
Ilic, D., Popovic, L. C., Ciroi, S., & Rafanelli, P. 2008, RMxAC, 32, 102
Jahoda, K., Markwardt, C. B., Radeva, Y., et al. 2006, ApJS, 163, 401
Jansen, F., Lumb, D., Altieri, B., et al. 2001, A&A, 365, L1
Kalberla, P. M. W., Burton, W. B., Hartmann, D., et al. 2005, A&A, 440, 775
Kayal, A., Singh, V., Ricci, C., et al. 2023, MNRAS, 522, 4098
Laha, S., Markowitz, A. G., Krumpe, M., et al. 2020, ApJ, 897, 66
Maiolino, R., Risaliti, G., Salvati, M., et al. 2010, A&A, 517, A47
Marchese, E., Braito, V., Della Ceca, R., Caccianiga, A., & Severgnini, P. 2012, MNRAS, 421, 1803
Marchesi, S., Ajello, M., Zhao, X., et al. 2019, ApJ, 872, 8
Marchesi, S., Zhao, X., Torres-Albà, N., et al. 2022, ApJ, 935, 114
Markowitz, A. G., Krumpe, M., & Nikutta, R. 2014, MNRAS, 439, 1403
Miniutti, G., Sanfrutos, M., Beuchert, T., et al. 2014, MNRAS, 437, 1776
Müller, A. L., Naddaf, M.-H., Zajaček, M., et al. 2022, ApJ, 931, 39
Nenkova, M., Ivezić, Ž., & Elitzur, M. 2002, ApJL, 570, L9
Nenkova, M., Sirocky, M. M., Nikutta, R., Ivezić, Ž., & Elitzur, M. 2008, ApJ, 685, 160
Netzer, H. 2015, ARA&A, 53, 365
Pizzetti, A., Torres-Albà, N., Marchesi, S., et al. 2022, ApJ, 936, 149
Pizzetti, A., Torres-Alba, N., Marchesi, S., et al. 2025, ApJ, 979, 170
Puccetti, S., Fiore, F., Risaliti, G., et al. 2007, MNRAS, 377, 607
Ramos Almeida, C., Alonso-Herrero, A., Levenson, N. A., et al. 2014, MNRAS, 439, 3847
Ramos Almeida, C., Esparza-Arredondo, D., González-Martìn, O., et al. 2023, A&A, 669, L5
Ricci, C., & Paltani, S. 2023, ApJ, 945, 55
Ricci, C., Ueda, Y., Koss, M. J., et al. 2015, ApJL, 815, L13
Ricci, C., Bauer, F. E., Arevalo, P., et al. 2016, ApJ, 820, 5
Risaliti, G., Elvis, M., Fabbiano, G., Baldi, A., & Zezas, A. 2005, ApJL, 623, L93
Risaliti, G., Elvis, M., & Nicastro, F. 2002, ApJ, 571, 234
Risaliti, G., Salvati, M., Elvis, M., et al. 2009, MNRAS, 393, L1
Rivers, E., Baloković, M., Arévalo, P., et al. 2015, ApJ, 815, 55
Sengupta, D., Torres-Albà, N., Pizzetti, A., et al. 2024, arXiv:2410.02878
Serafinelli, R., Braito, V., Reeves, J. N., et al. 2023, A&A, 672, A10
Tanimoto, A., Ueda, Y., Odaka, H., et al. 2019, ApJ, 877, 95
Titarchuk, L., Seifina, E., & Mishin, Y. 2024, arXiv:2411.09781
Torres-Albà, N., Marchesi, S., Zhao, X., et al. 2023, A&A, 678, A154
Torres-Albà, N., Marchesi, S., Zhao, X., et al. 2021, ApJ, 922, 252
Urry, C. M., & Padovani, P. 1995, PASP, 107, 803
Vander Meulen, B., Camps, P., Stalevski, M., & Baes, M. 2023, A&A, 674, A123
Verner, D. A., Ferland, G. J., Korista, K. T., & Yakovlev, D. G. 1996, ApJ, 465, 487
Zhao, X., Marchesi, S., Ajello, M., et al. 2021, A&A, 650, A57